MASTER'S THESIS

OPTIMIZATION OF IMAGE PROCESSING PROTOCOL ON HUMAN RESTING-STATE FMRI DATA

Gergely Dávid

Supervisors: Lajos R. Kozák, M.D, Ph.D.
assistant professor
MR Research Centre
Semmelweis University
Budapest

Szabolcs Dávid
physicist
Richter Gedeon Plc.
Budapest

Departmental Supervisor: Dávid Légrády, Ph.D.
associate professor
Institute of Nuclear Techniques
Department of Nuclear
Techniques

Budapest University of Technology and Economics
2014

ÖNÁLLÓSÁGI NYILATKOZAT

Declaration of independent work

Alulírott **Dávid Gergely** kijelentem, hogy jelen diplomamunkát önállóan, meg nem engedett segédeszközök igénybevétele nélkül készítettem. A diplomamunkában csak a megadott forrásokat használtam fel. Minden olyan részt, melyet szó szerint, vagy azonos értelemben, de átfogalmazva más forrásból vettem, a forrás megadásával egyértelműen jelöltem.

Kelt: Budapest, 2014.06.02.

...…….
Dávid Gergely

MŰEGYETEM 1782

Diplomamunka feladat a Fizikus mesterképzési (MSc) szak hallgatói számára

A hallgató neve:	**Dávid Gergely**	szakiránya:	**orvosi fizika**
A diplomamunkát gondozó (a záróvizsgát szervező) tanszék:			**Nukleáris Technika Tanszék**

A diplomamunka készítésének helye:	**Semmelweis Egyetem MRKK** **BME TTK Nukleáris Technika Intézet**		
A témavezető neve:	**Dr. Kozák Lajos Rudolf**	A konzulens neve:	**Dr. Légrády Dávid** (külső témavezető esetén kijelölt tanszéki munkatárs)
– munkahelye:	**Semmelweis Egyetem MRKK**		
– beosztása:	**egyetemi adjunktus**	– beosztása:	**egyetemi docens**
– e-mail címe:	**lkozak@mrkk.sote.hu**	– e-mail címe:	**legrady@reak.bme.hu**

A diplomamunka címe:	**Humán nyugalmi funkcionális MR adatok feldolgozási protokolljának optimalizálása**	azonosítója: **DM-2013-97**

A téma rövid leírása, a megoldandó legfontosabb feladatok felsorolása:

A korszerű MR technikák közé tartozó véroxigenizáció-szinthez kötött (ún. BOLD) funkcionális MRI (fMRI) alkalmas az idegrendszeri aktivitások követésére. Ez az eljárás indirekt módon, a vérkeringési válaszon keresztül következtet az idegi aktivitásokra. Segítségével lehetséges a központi idegrendszerben zajló folyamatok nem invazív, akár közel valós idejű nyomon követése, ezért ez a módszer különösen fontos az agykutatás szempontjából, a kognitív folyamatok megértésétől a gyógyszerkísérleteken át az orvosi alapkutatásokig.

Az utóbbi időben egyre nagyobb figyelmet kap az ún. nyugalmi fMRI, amely a nyugalomban lévő agy funkcionális hálózati kapcsolatainak mérésére ad objektív lehetőséget. Az MR képalkotás sajátosságai miatt ez a vizsgálat különösen érzékeny az alany elmozdulásaira, valamint különféle fiziológiai műtermékekre. Ezért az adatok kiértékelése előtt átfogó előfeldolgozási lépések alkalmazása szükséges.

A diplomamunka során a hallgatónak meg kell ismerkednie az MR képalkotás technikai és fizikai hátterén túlmutatóan az fMR képalkotás biológiai hátterével, különböző adatfeldolgozási technikákkal, valamint az eredmények interptetációinak lehetőségeivel és buktatóival. A jelölt feladatai:

- áttekintést nyújtani az fMR módszertan közelmúltbeli irodalmáról, különös tekintettel a nyugalmi fMR vizsgálatokra

- megvizsgálni a nyugalmi fMR adatokban található zajkomponensek jellemzőit, valamint azok lehetséges hatását a vizsgálat kimenetére

- végül pedig az adatfeldolgozási protokoll optimalizálása a zaj minél nagyobb fokú kiszűrése érdekében

A feladat kiadásának időpontja: **2013.02.04.**

Témavezető vagy tanszéki konzulens aláírása:	A diplomamunka témakiírását jóváhagyom (tanszékvezető aláírása):

Table of Contents

List of abbreviations

MRI	Magnetic Resonance Imaging
fMRI	functional Magnetic Resonance Imaging
rs-fMRI	resting-state functional Magnetic Resonance Imaging
FID	Free Induction Decay
SE	Spin Echo
EPI	Echo Planar Imaging
BOLD	Blood-oxygen-level dependent
TR	Repetition Time
TE	Echo Time
FOV	Field of view
oxy-Hb	oxyhemoglobin
de-Hb	deoxyhemoglobin
CBF	Cerebral Blood Flow
CBV	Cerebral Blood Volume
HRF	Hemodynamic Response Function
FWHM	Full width at half maximum
fc-MRI	functional connectivity magnetic resonance imaging
DMN	Default Mode Network
ROI	Region of interest
SCA	Seed-based Correlation Analysis
ICA	Independent Component Analysis
STC	Slice-timing Correction

GM	Grey Matter
WM	White Matter
CSF	Cerebrospinal Fluid
GLM	General Linear Model
aCompCor	anatomical Component based noise Correction
PCA	Principal Component Analysis
tSNR	temporal signal-to-noise ratio
LLP	Left Lateral Parietal lobe
RLP	Right Lateral Parietal lobe
PCC	Posterior Cingulate Cortex
MPFC	Medial Prefrontal Cortex
ATT	Dorsal Attention System

1. Introduction

Resting-state functional magnetic resonance imaging (resting-state fMRI) is a recent neuroimaging technique that is widely used to explore functional architecture of the brain. One of its main advantages is that it places a minimal cognitive burden on the participant and requires relatively little time in the scanner permitting data collection from populations that are typically difficult to study. The clinical potential of resting-state fMRI is significant, the possible applications are still being explored. While the method yields promising preliminary results in characterization of functional connections and in assessment of individual differences, there is a set of methodological questions that remains to be resolved. In the first part of the thesis, I briefly introduce the physical and physiological background of resting-state fMRI as well as the typical processing and analysis steps performed on the data. In the second part, the thesis addresses some of the unresolved issues and provides recommendations to optimize procedures for seed-based correlation analysis.

Resting-state fMRI signals are particularly susceptible to subject motion and other physiological artifacts resulting in an inherently low data quality. The high level of noise can lead to biased estimates of functional connectivity, which requires multiple preprocessing steps to be performed on the raw data. Several studies have used linear regression methods for data processing [1][2], however, at present, there is no clear consensus regarding the best approach. This lack of consistency in terms of preprocessing methods makes it difficult to compare resting-state fMRI studies, as different approaches can yield significantly different results. During my thesis project, I first explored the basic characteristics of the signal to get a better understanding of the nature of human resting-state data sets. Then, in an attempt to find an optimal protocol, I systematically tested the effects of several linear regression based preprocessing strategies on the sensitivity and specificity of functional network detection with particular focus on the anatomical component based noise correction.

I also investigated the effect of residual motion present after data preprocessing. Head motion is particularly challenging problem in resting-state fMRI studies, since it can significantly affect the output of the analysis even within the range of motion exhibited by typical, healthy young adults [3]. Furthermore, I tested the ability of a recently introduced frame censoring technique referred to as “scrubbing” [4] to eliminate residual motion effects.

Finally, the optimized data preprocessing and analysis protocol was applied to a clinical problem, where individual connectivity differences in patients with removed retrosplenial tumors were assessed.

2. Principles of magnetic resonance imaging

Magnetic resonance imaging (MRI) is an imaging technique used to investigate structure and function of the body. MRI has a wide range of applications in the medical diagnosis from neuroimaging through cardiovascular MRI to real-time MRI. The success of MRI lies in its numerous advantages compared to other imaging techniques. First, it does not involve exposure to radiation and no chemicals need to be injected into the body (if no contrast agent is applied). The health risks of an MR examination are therefore incomparably lower than that of most other radiological techniques. Second, MRI has an excellent soft tissue contrast, which is particularly useful for imaging soft tissues such as the brain or heart. Third, multiple contrast mechanisms can be exploited by MRI making it the most versatile imaging technique in medical diagnosis. Furthermore, the most important acquisition parameters (resolution, field of view, slice thickness, slice orientation etc.) are adjustable allowing the investigator a large degree of freedom in optimizing the settings to the particular application.

MRI is based on the quantum mechanical phenomenon of nuclear magnetic resonance, in which certain atomic nuclei absorb and subsequently emit electromagnetic radiation in the presence of an external magnetic field. Detection of the emitted radiation allows inferences about the properties of the investigated tissue. Section 2.1 introduces the magnetic moment of atomic nuclei, which gives rise to nuclear magnetic resonance. The Bloch equations that describe the dynamics of the magnetic moments under the effect of magnetic field are discussed in Section 2.2. These equations allow a purely classical description of the inherently quantum mechanical phenomenon.

MRI examinations involve simultaneous application of external magnetic field, radiofrequency (RF) pulses, magnetic gradient waveforms and data acquisition. Pulse sequences are used to manipulate magnetic moments in order to produce the desired signal. Section 2.3 describes two basic pulse sequences: free induction decay (FID) and spin echo (SE) sequences that are important to understand more advanced sequences.

Spatial encoding of the emitted RF signal is achieved by the application of magnetic gradients in multiple directions. The effect of these gradients on the measured signal and the process of generating spatial images are simpler to understand using the k-space concept, described in Section 2.4. In the last section, the pulse sequence of Echo Planar Imaging (EPI) is discussed, which plays a crucial role in neuroimaging with its use for virtually all functional MRI and diffusion imaging.

2.1 Nuclear magnetic resonance

The constituents of the atomic nucleus – protons and neutrons – possess angular momentum ($\vec{\boldsymbol{I}}$) that is the sum of orbital and intrinsic angular momenta (also known as spin). Further, the angular momentum of the nucleus is simply the vector sum of the individual angular momenta. Protons and neutrons have the tendency of forming pairs with zero resultant angular momentum, therefore only the unpaired protons and neutrons have contributions to the total angular momentum of the nucleus. In MRI, only nuclei with unpaired protons and/or neutrons are detectable because of their ability to produce magnetic resonance. Such nuclei include ^{1}H, ^{13}C, ^{23}Na, ^{31}P.

Nucleons have another property coupled to the angular momentum: the magnetic moment ($\vec{\boldsymbol{\mu}}$). The relationship between the two vector quantities is:

$$\vec{\boldsymbol{\mu}} = \gamma \vec{\boldsymbol{I}} \tag{1}$$

where $\vec{\boldsymbol{\mu}}$ and $\vec{\boldsymbol{I}}$ are the net magnetic moment and net angular momentum of the nucleus, respectively, and γ is the proportionality constant called gyromagnetic ratio. Gyromagnetic ratio is specific to the nucleus, for the nucleus of hydrogen its value is $42.58 \frac{MHz}{T}$.

Instead of investigating single nuclear magnetic moments, an intensive vector quantity, magnetization is defined as the sum of all magnetic moments in a given volume divided by the volume V itself:

$$\overrightarrow{\boldsymbol{M}}(\vec{\boldsymbol{r}}, t) = \sum_i \frac{\vec{\boldsymbol{\mu}}_{\boldsymbol{i}}(\vec{\boldsymbol{r}}, t)}{V} \tag{2}$$

In the absence of external magnetic field, the individual magnetic moments are randomly oriented; the net magnetization of a sample is zero. However, in the presence of external magnetic field the magnetic moments ($\vec{\boldsymbol{\mu}}$) interact with the $\vec{\boldsymbol{B}}_{\boldsymbol{0}}$ external field, creating a potential energy E dependent on the relative orientation of the two vectors:

$$E = -\vec{\boldsymbol{\mu}}\vec{\boldsymbol{B}}_{\boldsymbol{0}} \tag{3}$$

The rules of spin algebra also apply to magnetic moments, their projection onto the direction of external field can therefore only take on discrete values. If the z axis is defined as the direction of $\vec{\boldsymbol{B}}_{\boldsymbol{0}}$, the z component of the magnetic moment is:

$$\mu_z = \gamma I_z = \gamma \hbar m_I \tag{4}$$

where m_I is the magnetic quantum number of the nucleus and ħ is the reduced Planck constant. m_I can take on $2I + 1$ distinct values with I being the spin quantum number of the nucleus:

$$m_l = -I, -I + 1, \dots, I - 1, I \tag{5}$$

Thus, the potential energy values the particular nucleus can take on are also discrete:

$$E = -\gamma\hbar m_I B_z \tag{6}$$

In the case of ^{1}H nucleus the spin quantum number is ½, hence there are two energy states: $E_\uparrow$ for the spins pointing parallel to the magnetic field and $E_\downarrow$ for spins pointing antiparallel to that.

$$E_\uparrow = -\frac{1}{2}\gamma\hbar B_z \tag{7}$$

$$E_\downarrow = +\frac{1}{2}\gamma\hbar B_z \tag{8}$$

$$\Delta E = E_\downarrow - E_\uparrow = \gamma\hbar B_z = \omega\hbar \tag{9}$$

It follows from these equations that spins in alignment with $\vec{\boldsymbol{B}}_\mathbf{0}$ are in a lower energy state. The ratio between the occupation numbers of the two energy states is given by the Boltzmann equation:

$$\frac{N_\uparrow}{N_\downarrow} = e^{\frac{\Delta E}{kT}} \tag{10}$$

where k and T are the Boltzmann constant and the absolute temperature, respectively.

According to Equation (10) there is an excess number of spins in the lower energy state in equilibrium, resulting in a non-zero bulk magnetization in the z direction (M_z). The net magnetization in the $x-y$ plane is still 0, since there are no restrictions in this direction as was the case in the z direction. However, the equilibrium state of net magnetization can be perturbed because spins can change between energy states by absorbing or emitting energy. If the energy quantum of absorption is equal to the energy difference between the two energy-states given in Equation (9), the probability of absorption and induced emission increases by orders of magnitudes. The excitation of nuclear spins at a well-defined frequency is the nuclear magnetic resonance. As can be seen from Equation (9), the frequency of the selective excitation is magnetic field dependent:

$$f = \frac{\omega}{2\pi} = \frac{\gamma B_z}{2\pi} \tag{11}$$

Immediately after excitation the system begins to relax to the equilibrium state ($\vec{\boldsymbol{M}} = M_0\vec{\boldsymbol{z}}$). The relaxation in the z-direction is called T_1 relaxation (spin-lattice relaxation) and occurs by emitting energy quanta of the frequency as given in Equation (11). On the other hand, the relaxation in the $x-y$ plane (T_2 relaxation, spin-spin relaxation) is a process of losing phase coherence and it doesn't involve skipping energy levels.

2.2 Bloch equations

Bloch equations are a set of phenomenological equations describing the temporal behavior of magnetization. Let the magnetization be $\overrightarrow{\boldsymbol{M}}(t) = (M_x(t), M_y(t), M_z(t))$ with M_0 equilibrium magnetization in the z direction.The equations read:

$$\frac{\partial M_z(t)}{\partial t} = \gamma \left(\overrightarrow{\boldsymbol{M}}(t)\ x\ \overrightarrow{\boldsymbol{B}}(t)\right)_z - \frac{M_z(t) - M_0}{T_1} \tag{12}$$

$$\frac{\partial M_x(t)}{\partial t} = \gamma \left(\overrightarrow{\boldsymbol{M}}(t)\ x\ \overrightarrow{\boldsymbol{B}}(t)\right)_x - \frac{M_x(t)}{T_2} \tag{13}$$

$$\frac{\partial M_y(t)}{\partial t} = \gamma \left(\overrightarrow{\boldsymbol{M}}(t)\ x\ \overrightarrow{\boldsymbol{B}}(t)\right)_y - \frac{M_y(t)}{T_2} \tag{14}$$

The appearing T_1 and T_2 parameters are characteristic times describing the T_1 and T_2 relaxations. These parameters are tissue specific, therefore they present an important source of contrast. The two relaxation processes are independent from each other, but T_1 is always higher than T_2. Without relaxation the equations simplify to:

$$\frac{\partial \overrightarrow{\boldsymbol{M}}(t)}{\partial t} = \gamma \left(\overrightarrow{\boldsymbol{M}}(t)\ x\ \overrightarrow{\boldsymbol{B}}(\boldsymbol{t})\right) \tag{15}$$

If only the external magnetic field is present ($\overrightarrow{\boldsymbol{B}} = B_0\overrightarrow{\boldsymbol{z}}$), the equation describes a precession around the z axis with precession angular frequency of:

$$\omega_0 = \gamma B_0 \tag{16}$$

This equation is the Larmor equation and ω_0 is called the Larmor frequency and is equal to the frequency of energy quanta necessary to excite a spin.

Handling Bloch equations is much easier in a rotating reference frame. The effect of rotating reference frame is equivalent as if the spins experienced an effective magnetic field of $B_{eff} = B_0 - \Omega/\gamma$ along the z axis, where Ω is the angular frequency of the rotating frame rotating in the same direction as the precession of spins. In an appropriately selected rotating reference frame ($\Omega_0 = \gamma B_0$) the Larmor precession can be formally eliminated from the equations. Now, if an additional $\overrightarrow{\boldsymbol{B}}_1$ magnetic field (excitation field) is applied in the $x - y$ plane, the $\overrightarrow{\boldsymbol{M}}_0 = M_0\overrightarrow{\boldsymbol{z}}$ equilibrium magnetization begins to precess around the excitation field according to Equation (15). $\overrightarrow{\boldsymbol{M}}_{\boldsymbol{0}}$ can thus be rotated from the z direction by an angle of $\theta = \gamma B_1 t$.

In most pulse sequences, $\overrightarrow{\boldsymbol{M}}_{\boldsymbol{0}}$ is attempted to be flipped completely into the $x - y$ plane by turning on the excitation field for a proper period of time. In laboratory reference frame, the net magnetization vector (that has now transverse component) keeps rotating

around the external magnetic field during and after the excitation. This rotating magnetization induces voltage in the detector coils and is therefore detectable.

2.3 Basic pulse sequences

2.3.1 Free induction decay

Free induction decay (FID) is the simplest pulse sequence possible: the equilibrium M_0 magnetization is deflected to the transverse plane ($\theta = 90°$), where the initial magnetization ($M_\perp$) precess with its characteristic ω_0 Larmor frequency. The directly measurable signal S is proportional to the time derivative of the transverse magnetization. Without detailed derivation it can be formulated as:

$$S(t) \sim \omega_0 e^{-t/T_2^*} \int M_\perp(\vec{r}) e^{i(\omega_0 t + \phi(\vec{r},t))} d^3r \tag{17}$$

The above equation accounts for the local inhomogeneities in the spin ensemble, as well. According to Equation (17) a precessing magnetization vector generates a decaying harmonic signal in the detecting coil. The decay of the free induction signal is characterized by T_2^* that is made up of two factors:

$$\frac{1}{T_2^*} = \frac{1}{T_2'} + \frac{1}{T_2} \tag{18}$$

T_2' and T_2 refer to different relaxation processes. The relaxation characterized by T_2 is associated with the molecular-level random movement of the nuclei containing the magnetic moments; the dephasing caused by this process cannot be traced back. In contrast, the relaxation characterized by T_2' is caused by local inhomogeneities in the external magnetic field that force the spins at different locations to precess at different frequencies. The dephasing due to different precession rates manifests itself in signal loss that follows an approximately exponential pattern. The detected harmonic signal and the parameters characterizing the envelope of the signal can be seen in Figure 1.

2.3.2 Spin echo

With the application of spin echo (SE) sequence the effect of T_2' relaxation can be reversed. This is achieved by a 180° refocusing pulse that follows the 90° excitation pulse by a period of τ. During this period the spins precessing at different frequencies build up different phases that are linearly proportional to τ. The refocusing pulse negates the accumulated phases, which means that after another period of τ the spins eliminate their earlier accumulated phases. However, the dephasing caused by T_2 cannot be refocused, therefore the measured signal in an SE sequence depends on only T_2 (when measured at 2τ). The defining parameter

of this sequence is the echo time (TE) that represents the time between the excitation and the peak of the echo signal. The evolution of the detected signal in a spin echo experiment is displayed in Figure 2.

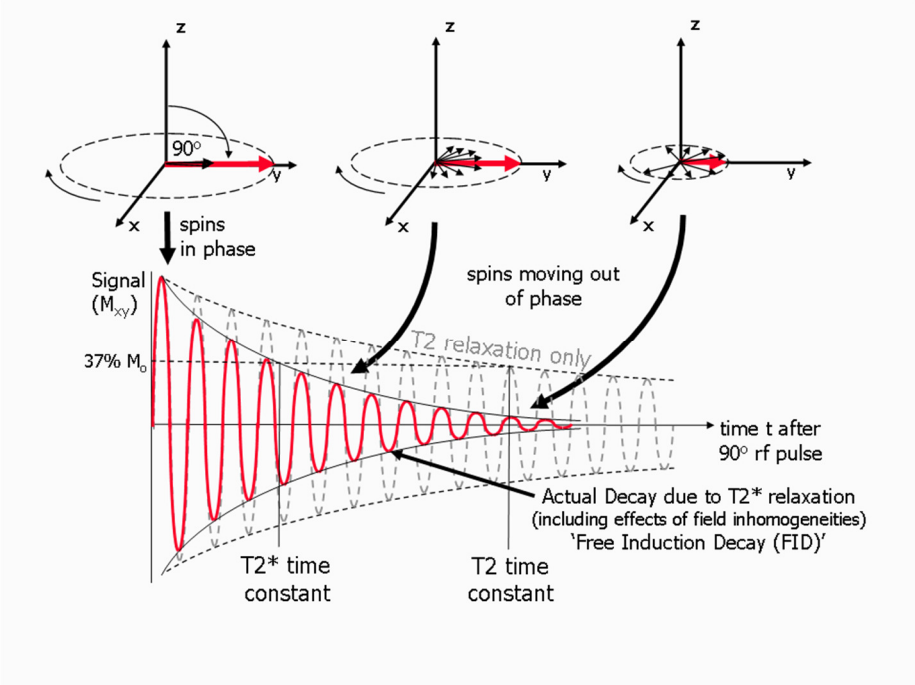

Figure 1. T_2 and T_2^* relaxation processes. The amplitude of the net transverse magnetization (and therefore the detected signal) decays as the proton magnetic moments move out of phase with one another (shown by the small black arrows) [5].

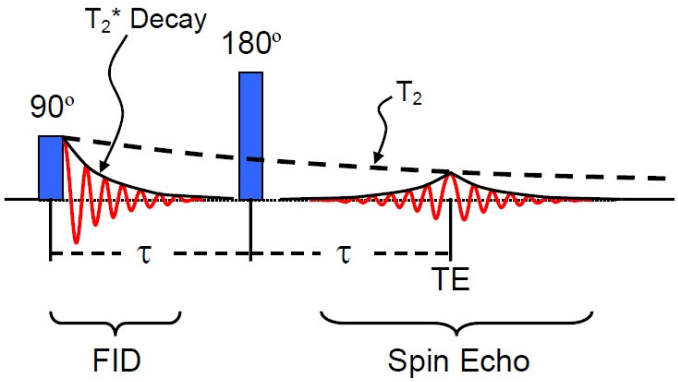

Figure 2. Scheme of generating spin echo. The 180° refocusing pulse applied at τ creates a signal maximum (spin echo) at 2τ [6].

2.4 Sampling of k-space

Equation (17) can be reformulated by assuming that the signal is demodulated to remove Larmor precession and there is no relaxation. Further, proportionality factors not specified in Equation (17) can be condensed with the initial transverse magnetization $M_\perp(\vec{r})$ into a single

component called effective spin density and denoted by ρ_{eff}. ρ_{eff} is also the function of $\vec{\boldsymbol{r}}$ and comprises factors that determine the local intensity of the signal including sensitivity of detecting coils, local magnetization, Larmor frequency etc. If relaxation is present, it can also be incorporated into ρ_{eff}. The time-domain signal created by transverse magnetization can thus be written as:

$$S(t) = \int \rho_{eff}(\vec{\boldsymbol{r}}) \cdot e^{-i\Phi(\vec{r},t)} d^3r \tag{19}$$

The accumulated phase (in radians) within time t and at location $\vec{\boldsymbol{r}}$ is:

$$\Phi(\vec{\boldsymbol{r}}, t) = \gamma \int_0^t \omega(\vec{\boldsymbol{r}}, t')dt' = \gamma \int_0^t \vec{\boldsymbol{r}} \cdot \vec{\boldsymbol{G}}\,(t')dt' \tag{20}$$

where $\vec{\boldsymbol{G}} = \nabla\omega$ is the gradient vector of the precessing frequency, and is therefore directly proportional to the gradient of the z component of the magnetic field. Let us define $\vec{\boldsymbol{k}}$ as:

$$\vec{\boldsymbol{k}}(t) = \frac{\gamma}{2\pi} \int_0^t \vec{\boldsymbol{G}}\,(t')dt' \tag{21}$$

With the definition of $\vec{\boldsymbol{k}}$, Equation (19) becomes:

$$S(t) = \int \rho_{eff}(\vec{\boldsymbol{r}}) \cdot e^{-2\pi i \vec{\boldsymbol{k}}(t)\cdot\vec{\boldsymbol{r}}} d^3r \tag{22}$$

From this form of Equation (22), it is evident that the measured signal $S(t)$ is the Fourier transform of the effective spin density $\rho_{eff}(\vec{\boldsymbol{r}})$. Since $\vec{\boldsymbol{k}}(t)$ is Fourier conjugate variable to $\vec{\boldsymbol{r}}$, it is practical to consider the signal as a function of $\vec{\boldsymbol{k}}$. The space that $\vec{\boldsymbol{k}}(t)$ resides in is known as k-space, and it has units of inverse distance, typically inverse centimeters. With evolving time $S\big(\vec{\boldsymbol{k}}(t)\big)$ traces a trajectory in the k-space. From Equation (21) it follows that the speed of k-space traversal is determined by $\vec{\boldsymbol{G}}$ and γ, and the trajectory in k-space is parallel to $\vec{\boldsymbol{G}}$.

The goal of all pulse sequences is to sample the k-space by introducing magnetic gradients in multiple directions. After sampling with an appropriate field of view and density is achieved, the measured signal is inverse Fourier transformed to obtain the effective spin density map in the native $\vec{\boldsymbol{r}}$ space. Note that resulting from the Fourier conjugate properties, the resolution and field of view in the native space are numerically the inverse of the field of view and resolution in the k-space, respectively. To create a 3D image, k-space traverse in 3 mutually orthogonal directions is necessary. However, most pulse sequences reduce the problem of 3D imaging to 2D by building up the volume from sequentially sampled slices. The slices are excited selectively by the so-called slice selection gradient (G_z) applied in the z direction. Subsequent sampling of the selected slice is achieved by two additional imaging gradients, the phase encoding and the frequency encoding gradient that are applied in the x

and y directions. The time between successive excitations applied to the same slice is the repetition time (TR).

2.5 Echo planar imaging

One of the main advantages of the k-space concept is that sampling strategies of different sequences can be illustrated in a very descriptive manner. As an example I briefly introduce the idea behind echo planar imaging (EPI) sequence outlining which characteristics of the acquisition strategy make it one of the fastest pulse sequences.

The pulse sequence diagram of EPI can be seen in Figure 3A., where the lines of **G_z**, **G_y** **G_x** refer to the application of imaging gradients in the x, y, z directions, respectively, while the lowest line represents the evolution of the signal measured in the acquisition periods. The k-space traversing pattern dictated by the order, direction and magnitude of gradients is illustrated in Fig.3B. Note that EPI samples the whole 2D k-space after a single excitation by applying a series of bipolar gradients that creates a zig-zag sampling pattern in k-space. This sampling strategy is in contrast to conventional sequences, in which only one k_y line is acquired after an excitation, making the sampling considerably slower. Also note that EPI lacks 180° refocusing pulses, echoes are formed by bipolar gradients in the frequency encoding direction. It means that the measured signal evolves under the envelope of T_2^* relaxation, which makes the sequence sensitive to susceptibility differences such as BOLD contrast described in Section 3.1.

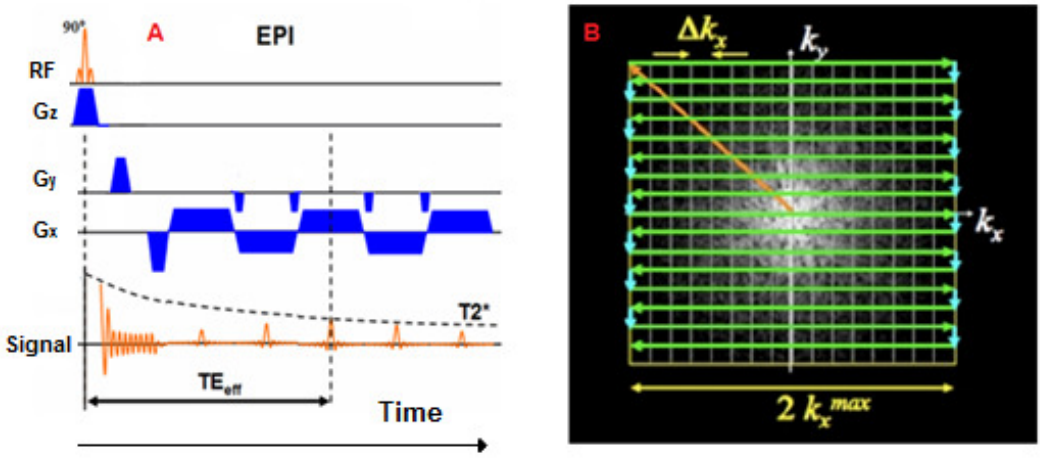

Figure 3. A: Schematic illustration of the 2D EPI pulse sequence [7]. The first channel (RF) represents the application of radiofrequency excitation, the middle three channels the application of gradient waveforms in three orthogonal directions over time. The last channel depicts the temporal evolution of MR signal, where TE_{eff} is the effective echo time corresponding to the acquisition of the middle k_y line. B: Sampling pattern of the k-space [8].

3. Functional magnetic resonance imaging

In a broader sense functional magnetic resonance (fMRI) refers to a series of MRI techniques with the common goal of obtaining functional information from living organisms. These methods include without the claim of completeness functional brain mapping, diffusion and perfusion techniques. However, in the commonly used narrower sense of the word only the functional brain mapping techniques are termed as fMRI.

Functional brain mapping attempts to detect and localize neural activity by creating contrast between active and passive states of neuronal ensembles within the central nervous system. All of these methods rely on the fact that neuronal activations and cerebral blood flow are coupled. There are several relevant contrast mechanisms for measuring associated changes in the blood flow. Contrast agent administration into the cerebral bloodstream is an invasive method and has not found widespread use. Since the early 1990s the Blood-oxygen-level dependent (BOLD) contrast is the dominant source of contrast in fMRI studies, which uses deoxyhemoglobin as an endogenous contrast agent [9]. Due to its dominant role BOLD-fMRI is often referred to as simply fMRI in the literature, whereby I also follow this practice throughout the thesis. Section 3.1 briefly summarizes the physiological and physical basis of BOLD contrast and also discusses its limitations. Arterial spin labeling is also a commonly used neuroimaging technique that can provide useful complementary information to BOLD-fMRI, but its discussion is beyond the scope of this thesis.

While task-based fMRI studies[1] has significantly contributed to our understanding of human brain function, there is a rapidly growing interest in resting-state fMRI (rs-fMRI), which can provide new insights on the functional architecture of the brain. Section 3.2 discusses the motivation behind the acquisition of rs-fMRI and introduces the concept of resting-state networks.

3.1 BOLD contrast

BOLD contrast represents a non-invasive, indirect measure of neural activity induced by a complex interaction of physiological and physical factors. Understanding these factors is critical to the selection of proper pulse sequences and to the interpretation of BOLD-fMRI results.

[1] Task-based fMRI refers to the experimental design where neuronal activations evoked by external stimuli (experimental paradigm) are detected.

3.1.1 Physical basis

BOLD-fMRI relies on the fact that magnetic properties of oxyhemoglobin (oxy-Hb) and deoxyhemoglobin (de-Hb) are different. While oxyhemoglobin is a diamagnetic compound with a very small negative magnetic susceptibility ($\chi \approx -10^{-5}$), deoxyhemoglobin is a paramagnetic molecule due to its unpaired electrons with a significantly higher magnetic susceptibility ($\chi \approx 10^{-4}$). Since brain tissues also possess diamagnetic properties (due to their dominant water content), deoxyhemoglobin substantially distorts the external magnetic field present in the brain, which in turn results in a more rapid spin-spin relaxation in the surrounding tissue. It means that the T_2^* relaxation time in and around the blood vessels[2] depends on the level of deoxyhemoglobin, where a decreased amount of deoxyhemoglobin causes a slower dephasing associated with a higher T_2^*. Thus, pulse sequences sensitive to T_2^* effect show higher signal where blood is more oxygenated.

The effect of dephasing scales with the square of the magnetic field, high magnetic fields (1.5T or higher) are therefore desirable for fMRI studies. An important aspect of the imaging sequence is that it must be T_2^*-weighted. Therefore, gradient echo sequences are dominantly used but spin echo sequences still show BOLD contrast because of diffusion effects. The amount of T_2^*-weighting in the image is determined by the echo time (TE). To obtain maximal difference between oxygenated and deoxygenated blood, the optimal value of TE must be equal to the T_2^* of the particular tissue. However, in practice a lower TE is usually used to reduce signal dropouts due to magnetic inhomogeneities (see Fig.4). Besides T_2^* sensitivity, applied sequences must also allow a rapid image acquisition. Most research is carried out using gradient-echo EPI sequences (see Section 2.5), because they satisfy the aforementioned criteria.

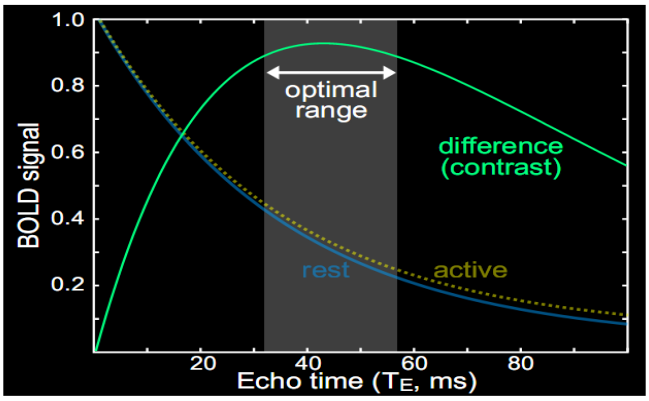

Figure 4. Optimal echo time for BOLD imaging [10].

[2] Since arteries are fully oxygenated, BOLD effects take place only in the venous part of the blood stream, resulting in a venous nature of BOLD contrast.

3.1.2 Physiological basis

In the early 1990s, Seiji Ogawa et al. have demonstrated that the local amount of deoxyhemoglobin (deHb) can be used to detect neuronal activity [9]. Brain activation triggers a complex sequence of cellular, metabolic and vascular processes that influence the deHb-level around firing neurons and give rise to BOLD contrast.

Upon neuronal firing, energy is required for the maintenance and restoration of neuronal membrane potentials. Since the internal stores of energy in the form of glucose and oxygen are scarce, energy must be continuously provided by the blood supply to the brain. Although the mechanism of the link between neuronal activity and blood flow is still under investigation, it is generally understood that neuronal activity is closely coupled with local cerebral blood flow through a chain of physiological processes known as neurovascular coupling. Neurovascular coupling tries to compensate the increased energy demand associated with neural firing by increasing the local cerebral blood flow (CBF) and – to a smaller extent – the cerebral blood volume (CBV).

The hemodynamic response of the brain temporally changes the local amount of deHb as illustrated in Figure 5A. The figure shows the temporal behavior of several physiological parameters following neuronal firing. Immediately after the onset of stimulus, the cerebral metabolic rate of O_2 ($CMRO_2$) increases by appr. 5% to meet the increased energy demand of neurons. Extracting more O_2 from the blood raises the local deHb amount resulting in an "initial dip" of the MR signal between 0 and 2 s. Due to the slower process of neurovascular coupling, the increase of cerebral blood flow lags the progression of $CMRO_2$, but the increase of CBF by appr. 50% far exceeds that of $CMRO_2$. Thus, the demand on oxygenated blood is overcompensated by the higher CBF resulting in a smaller local amount of deHb. Eventually, the reduction of deHb amount leads to an improved T_2^*-weighted signal (BOLD signal) since the more diamagnetic blood interferes with the external magnetic field less (T_2^* is higher).

In summary, the BOLD signal is the result of a series of physiological and physical processes, which are often only partially understood. However, early studies have shown that the participating factors can be modeled as a linear system with the input of neural stimulus and output of T_2^*-weighted signal [11]. This linear system has a known impulse response function called hemodynamic response function (HRF) in this context. Figure 5B shows a typical HRF, which reflects the signal behavior in response to a brief neuronal firing. The signal rises to a peak over 4–6 seconds, before falling back to the original level (and typically undershooting slightly).

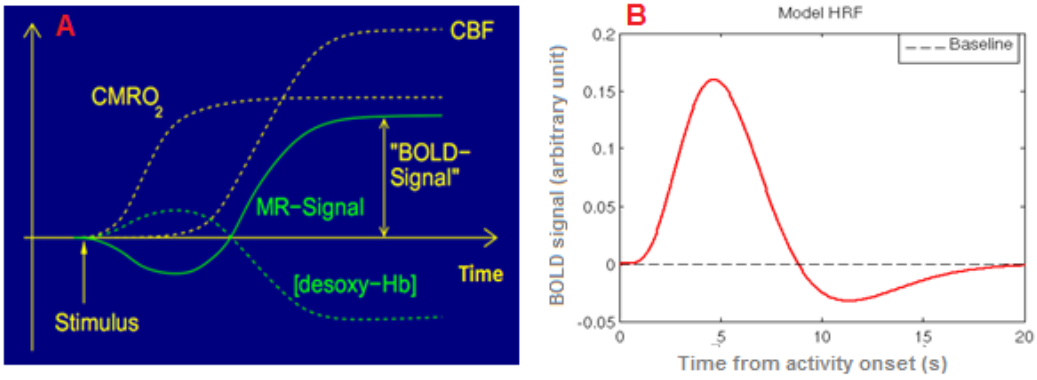

Figure 5. A: Schematic temporal behavior of several physiological parameters and the BOLD signal after the onset of a continuous stimulus [12]. B: Hemodynamic response function modeled as the sum of two gamma functions [13].

3.1.3 Limitations

Although most fMRI studies use BOLD contrast due to its non-invasive nature, relatively high spatial resolution and contrast-to-noise ratio, and due to easily implementable measurements, there are several limitations of the method. First, BOLD-fMRI only allows an indirect measurement of neural activity through the deHb level of the cerebral vasculature. Intra- or intersubject differences of vascular properties (CBF, CBV) can lead to biased findings in task- and resting-state fMRI (for further discussion see Section 4.2.2).

Other limitations come from the spatial and temporal properties of the HRF. The spatial effect of HRF on the signal is similar to a spatial blurring, where the full width at half maximum (FWHM) is magnetic field dependent and is around 3 mm at 3T [14]. This blurring is primarily due to large veins that drain extended areas and can exhibit higher changes in the deHb amount than smaller capillaries despite larger distance from the location of activation. As can be evident from Figure 5B, HRF also represents a temporal smoothing of the neuronal firing pattern, since the signal rises and falls within an interval of appr. 20 s in response to a single stimulus.

3.2 Resting-state fMRI

Human brain is constantly active even when the subject is not performing any explicit task. The detection of resting-state brain activity by BOLD contrast is referred to as resting-state fMRI, and in recent years this technique has proven to be a powerful method to describe functional architecture of the brain [15].

3.2.1 Resting-state fMRI signal

The intensity time series of a given voxel acquired by BOLD fMRI shows fluctuations even in the absence of external stimuli. These spontaneous, resting-state fluctuations ("BOLD fluctuations") are associated with the baseline activity of the human brain and have been found to exhibit synchronous behavior among distant parts of the brain. Biswal et al. were the first to demonstrate such coherent BOLD signal intensities between contralateral motor cortices [16]. Figure 6 displays a replication of the coherent signal behavior between left and right motor cortices in one of our participants (for details about subjects, see Section 5.1).

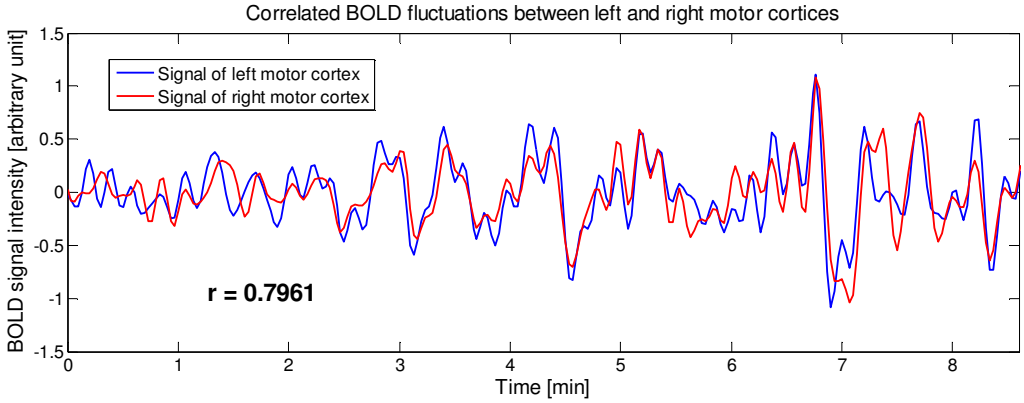

Figure 6. Averaged BOLD signals in the left and right motor cortices. The high association between the two signals are evident, reflected in a correlation coefficient of r=0.7961.

Many similar observations of spontaneous low-frequency fluctuations have led to the introduction of the concept of functional connectivity. Functional connectivity is defined as temporally correlated remote neurophysiological events [17][18], where it is not explicitly required that one event is influencing the other. A distinction must be made between functional and anatomical connectivity (as measured by diffusion methods), but accumulating evidence suggests that functional connections are sufficiently constrained by anatomy [18] and coherent low-frequency fluctuations relate to known anatomical systems.

3.2.2 Resting-state functional networks

The goal of measuring functional connectivity MRI (fc-MRI) is to identify connectivity patterns within and between distinct brain systems. These patterns are known as "intrinsic connectivity networks" or "resting-state networks[3]". Figure 7 displays some functional systems including visual and auditory systems [20][21], the default mode network [1], the

[3] The term resting-state is often used in the context of functional networks because they are most often measured at rest. However, it doesn't mean that resting-state has a special status that maximizes the presence of coherent fluctuation in all systems.

working memory system [1], and the executive control network [21] that have consistently been found across subjects and across a range of analysis techniques.

Functional networks have been demonstrated to be present during task-based paradigms and in varied states of consciousness. They persist during sleep [22] and anesthesia [23], suggesting they reflect, to a large degree, intrinsic processes. In addition, studies show differences across the lifespan, between individuals with clinical diagnoses, and across varied personality traits [24]. Functional connectivity measures may therefore serve as an indicator for psychiatric and neurological disorders, possibly allowing for improved early detection of such dysfunctions in the brain.

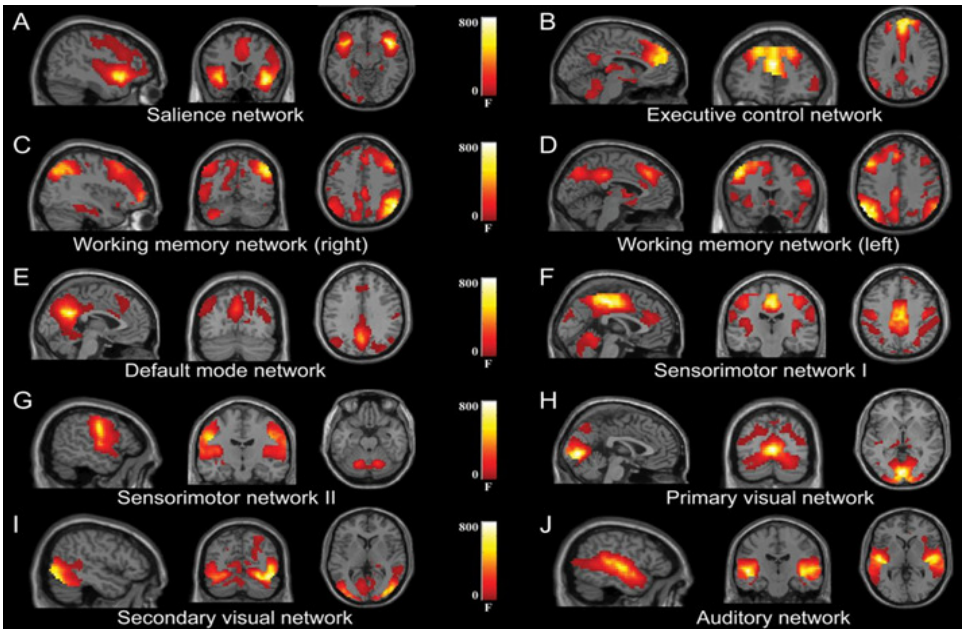

Figure 7. Resting-state functional networks identified by group-level independent component analysis [19].

It is generally accepted that human brain consists of interacting systems of anatomically connected areas. Furthermore, studies have hypothesized that there are two opposed, widely distributed brain systems, one consisting of regions routinely exhibiting task-related activations such as somatosensory, visual or attention network, and the other consisting of regions routinely exhibiting task-related deactivations such as default mode network (DMN) [1]. Terms used to refer to these systems are “task-positive” and “task-negative”. The DMN is probably the most studied network, and is associated with cognitive functions including autobiographical memory, envisioning the future, theory of mind and moral decision making [25].

4. Processing and analysis of resting-state fMRI data

There are two major analysis approaches used for assessing functional connectivity in resting state data: seed-based correlation analysis (SCA) and independent component analysis (ICA). However, raw[4] fMRI data require several manipulations, known as preprocessing steps prior to applying any analysis method. Spatial and temporal preprocessing steps are necessary to correct for spatial and temporal inconsistencies present in all fMRI data and caused by several factors such as physiological oscillations, subject head motion, inhomogeneities in the static magnetic field, timing differences of image acquisition etc. If uncorrected, these factors can seriously confound individual and group-level functional connectivity results. In Section 4.1 a series of computational procedures are described which are typically applied to both task- and resting-state fMRI data and operate (with exception of slice-timing-correction) in the spatial dimension of the data. Section 4.2 discusses the aforementioned seed-based correlation analysis with its properties, advantages and disadvantages. Since this method is particularly vulnerable to noise in the time domain, multiple temporal preprocessing steps are applied in order to reduce spurious noise and increase validity of the analysis. Section 4.3 describes the most commonly used temporal preprocessing steps in the context of resting-state data analysis (regression of nuisance signals and frequency filtering) highlighting the potential interpretative issues associated with these procedures. Seed-based correlation analysis is performed on data that have already undergone temporal preprocessing in order to minimize structured noise. In this chapter discussion of SCA precedes that of temporal preprocessing in an attempt to introduce the motivation why temporal processing needs to be included in the processing stream.

4.1 Spatial preprocessing

The processing steps discussed in this section can be performed using multiple software tools and packages that may implement these computational procedures somewhat differently. Since I used SPM8[5] software [26] throughout my analyses, I focus on describing these methods as implemented in this software. In this section only the key concepts of the spatial processing steps are explained, the exact order of steps and applied parameters are given in Section 5.2. Note that despite being a temporal processing step, slice-timing correction is also

[4] Raw time series refers to the temporal dimension of the acquired and reconstructed dataset, on which only spatial manipulations have been performed (see Section 4.1).

[5] Statistical Parametric Mapping (SPM) software, Wellcome Department of Cognitive Neurology, London, UK, (www.fil.ion.ucl.ac.uk/spm/software/spm8/).

covered in this section because it is highly integrated into the spatial processing stream and it is not specific to resting-state data preprocessing.

4.1.1 Slice-timing correction

Functional MRI data are usually acquired using repeated two-dimensional pulse sequences like echo planar imaging that limit the effect of the excitation pulse to a single slice using the slice selection gradient (see Section 2.5). Therefore, slices of functional images are acquired at different time points throughout the repetition time. Depending on the TR and the slice scanning order[6] (sequential/interleaved), these delays between individual slices may add up to significant temporal shifts over the 3D volume. To compensate for the temporal offsets between individual slices, slice-timing correction (STC) is applied to the functional data.

In slice-timing correction, the individual slices are temporally realigned to a reference slice based on its relative timing using an appropriate resampling method. Figure 8 illustrates the temporal interpolation of individual slices to the reference slice (first slice) in both sequential and interleaved scanning order. The standard interpolating method is usually sinc interpolation.

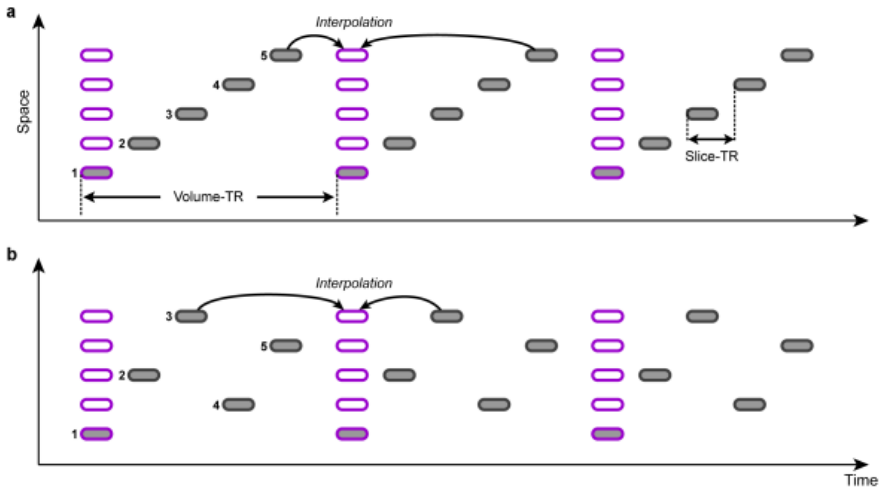

Figure 8. Schematic illustration of slice-timing correction using **a**: sequential and **b**: interleaved slice scanning order. Acquired data points are interpolated to the time point of the reference slice (first slice in this case) [27].

[6] Slice scanning order is the order in which individual slices of a volume are scanned. One approach is to use sequential ascending/descending slice acquisition, in which slices are acquired sequentially. Using interleaved scanning order the odd slices are recorder first followed by the even slice number (or vice versa) in order to avoid cross-slice excitation.

4.1.2 Realignment and the issue of head motion

Head motion is a significant confound that can reduce the validity of fMRI studies and limit the effectiveness of the method. Despite the use of immobilization devices head motion can't be fully eliminated due to long scan durations and the restrictive environment within the scanner. Furthermore, small head movements due to physiological processes including breathing, swallowing, etc. are also always present.

The aim of using motion correction is to remove movement artifacts in fMRI time series, which can seriously degrade the quality of the data especially at the tissue boundaries including the edges of the brain. All of the fMRI analyses assume that each voxel uniquely represents a portion of the brain, which is not true anymore in the presence of head motion.

Realignment attempts to correct for these head displacements by realigning subsequently acquired volumes to a reference volume using a least squares approach and a 6 parameter rigid-body (three translation and three rotation parameters) transformation. The six parameters are estimated iteratively by analyzing how the source volume should be transformed in order to better match the reference volume. Following the optimization procedure the estimated motion parameters can be applied to the source volume to spatially resample the uncorrected volumes using an appropriate interpolating algorithm (usually a 3rd degree B-Spline interpolation). Figure 9A shows an example of the estimated motion parameters representing the translational and rotational displacements relative to the first volume. In contrast, Figure 9B illustrates the differential displacements as compared to the previous volume. Note that sudden movements are much easier to identify in the differential plot.

Realignment alone is not sufficient to fully eliminate the effects of head motion. Although spatial displacements can be reliably corrected in image space, head motion also results in intensity changes in fMRI time series, which is particularly problematic in resting-state fMRI, where the temporal signal-to-noise ratio[7] is inherently low. First, movement of the head disturbs the homogeneous magnetic field that has been fine-tuned at the beginning of the scan session by "shimming". This perturbation leads to unpredictable signal loss and image distortion in subsequent images. Second, since spins are excited sequentially slice-by-slice, motion in the slice selection direction changes the spin saturation profile in the acquired 2D slice. The resulting effect is called "spin history effect" because the signal intensity of a particular voxel depends on the history of excitation experienced by spins in this volume.

[7] Temporal signal-to-noise ratio (tSNR) is defined as the ratio of the mean of a time series to its standard deviation.

Besides these two prominent examples there are a couple of other mechanisms that contribute to head movement induced artifacts.

In summary, motion-related intensity changes make motion one of the most damaging and frustrating problem for resting-state fMRI studies. Intensity-related effects of head motion and possible corrections are discussed in more detail in Section 5.6.

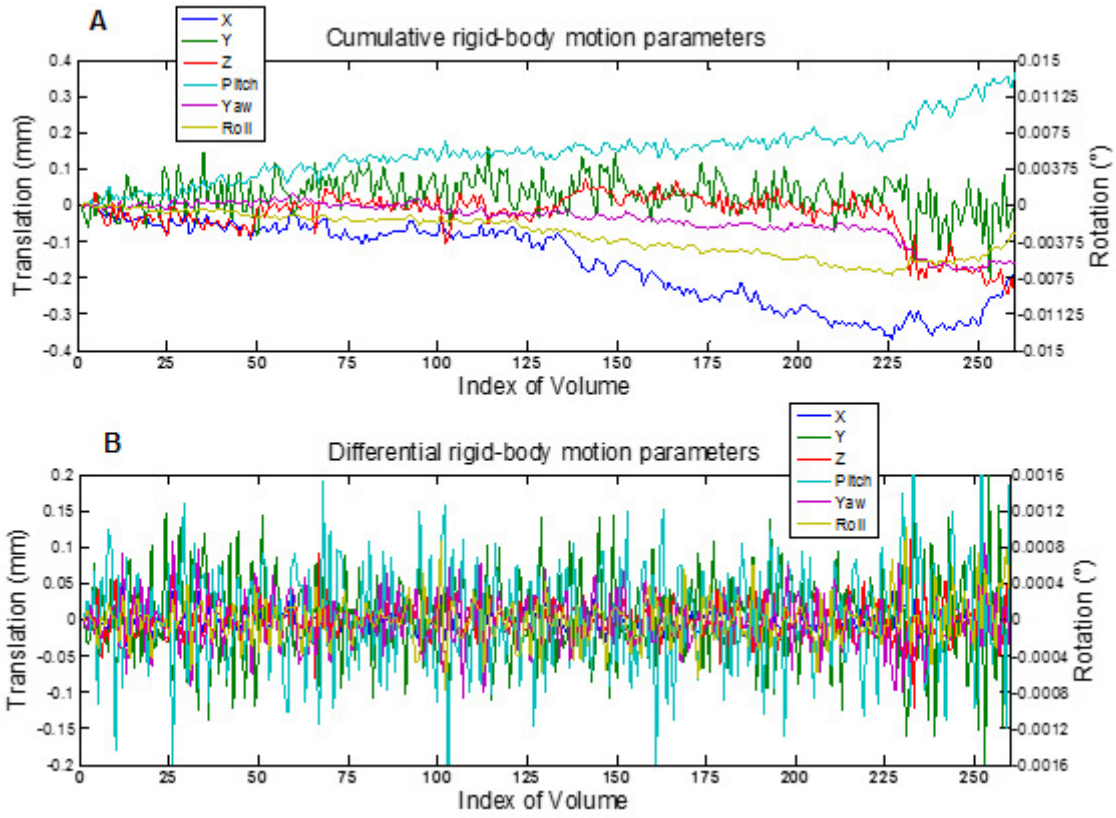

Figure 9. A: Six realignment parameters of a subject estimated by SPM. The three translational parameters (X, Y, Z) are scaled in mm on the left y-axis, the three rotational parameters (Pitch, Yaw, Roll) in ° on the right y-axis. B: Time derivative of the realignment parameters calculated by backward difference.

4.1.3 Coregistration

Spatial coregistration is an intrasubject registration that aligns functional (usually the mean motion corrected image) and anatomical images of the individual subjects, so that functional data can be superimposed onto the correct anatomical location. Coregistration is usually based on the same rigid-body model discussed in the previous section; however, the cost function used during the iteration step is not the least sum of squares if the functional and anatomical images have different modalities. In this case mutual information is maximized; this approach works without the assumption that intensities of images to be coregistered match. Since the

number of iterations is limited, the images need to be approximately in the same location/orientation prior to coregistration.

4.1.4 Segmentation

Segmentation creates within-subject tissue probability maps for grey matter, white matter and cerebrospinal fluid using the high-resolution contrast-rich T_1 weighted anatomical image and a priori information regarding the probability of a tissue type at each location. Individual segmented images are key to define grey matter masks for the functional connectivity analyses and to determine "noise regions" from which noise regressors are extracted (see Section 4.3.4). In SPM, segmentation is performed simultaneously with spatial normalization (next section) within the framework of the unified segmentation and normalization algorithm [28].

4.1.5 Normalization

The human brain shows remarkable variability in its shape and morphology. However, it is essential for a group analysis that every subject's brain is of the same size and orientation. In order to make individual brains comparable, the images (both functional and anatomical) are registered to a standard space[8] through spatial normalization. Normalization involves minimization of the sum of squared differences between the template image and the source image of the same modality. In contrast to realignment and coregistration, normalization changes the size of the brain using a 12-parameter affine transformation. Usually a global non-linear warping algorithm is also applied in order to match the size and position of the template. The process of normalization and resampling is sometimes accompanied by changing the voxel size.

Images are transformed into a common space through normalization where functionally homologous areas from different brains are as close as possible. However, there can still be anatomical differences among subjects. In addition, function and structure don't match exactly resulting in a degraded inter-subject functional overlap. These factors can be (partially) compensated by blurring the normalized functional images.

[8] There are two widely accepted standard stereotaxic coordinate spaces: Tailarach and MNI. These templates differ in size, shape and representativeness. Talairach brain is derived from one post-mortem brain of a 60-year old woman and it has often been criticized for its suboptimal representativeness. The more commonly used MNI152 template of the Montreal Neurological Institute is derived from 152 T_1-weighted images and is more representative for the population. Both stereotaxic spaces have their origin in the midpoint of the anterior comissure.

4.1.6 Spatial smoothing

Smoothing is performed by blurring functional images with a typically Gaussian filter characterized by its full-width-at-half-maximum (FWHM). Spatial smoothing serves multiple purposes. Besides increasing the signal-to-noise ratio by suppressing high spatial frequency noise, it increases the functional overlap among subjects and thus compensates for the slight differences between the functional and anatomical data. In resting-state fMRI analysis, spatial smoothing also has an impact on the calculated functional connectivity measures. In most cases the effect of smoothing is not critical since time series are averaged within a defined region. However, in the absence of averaging or in case of a small ROI spatial smoothing can significantly improve group-level results.

4.2 Analysis methods

There is a rich toolkit of analyzing preprocessed fMRI data in the literature, ranging from simple bivariate measures characterizing the similarity between voxel or ROI time series at multiple locations through graph theoretical measures to sophisticated multivariate exploratory techniques such as Independent Component Analysis. These methods use highly different approaches, assumptions and thus capture different aspects of the human brain function. Within the framework of the thesis I exclusively used seed-based correlation analysis, since this is the most widely applied and most easily interpretable measure of synchronicity in brain function. Besides, it was shown on simulated and human fMRI data, that correlation can be quite successful in terms of sensitivity to network connection detection in contrast to higher-order statistics and lag-based approaches [29].

4.2.1 Seed-based correlation analysis

Seed-based correlation analysis is based on calculating cross-correlation coefficients among time series of voxels (or ROIs). In practice and throughout the thesis Pearson's product-moment correlation coefficient is used, which is shortly referred to as "correlation coefficient" and denoted by r. It is a dimensionless bivariate measure describing the linear statistical dependence between two variables or time series. Correlation coefficient for a sample is the scaled version of the covariance between two time series and takes values between -1 and 1. It is given by the following formula:

$$r = \frac{\sum_{i=1}^{n}(X_i-\bar{X})(Y_i-\bar{Y})}{\sqrt{\sum_{i=1}^{n}(X_i-\bar{X})}\sqrt{\sum_{i=1}^{n}(Y_i-\bar{Y})}} \tag{23}$$

where X_i and Y_i denote the two signals to be correlated at time point i, $\overline{X}$ and $\overline{Y}$ are the average signals over the course of the measurement and n is the number of the data points involved in the analysis.

Seed-based correlation analysis requires strong a priori assumptions for the selection of a voxel or ROI from which time series are extracted. This extraction is straightforward in case of a single seed voxel; however, when using a ROI as a seed an estimator of the regional activity is needed as well, which is typically the average signal within the ROI. Correlating every seed's time series with all of the other seeds' time series can create voxel-wise or parcellated whole-brain functional connectivity maps, sometimes referred to as functional connectome in contrast to anatomical connectome as measured by diffusion-based methods.

For group-level SCA, subject-level sample correlation coefficients are Fisher transformed as follows:

$$z = \frac{1}{2}\ln\left(\frac{1+r}{1-r}\right) \tag{24}$$

Fisher transformation facilitates hypothesis testing about the value of the population correlation coefficient ρ between two variables by making sample correlation coefficients approximately normally distributed.

4.2.2 Advantages and pitfalls

The SCA method has proven to be useful in identifying several functional networks spanning across the brain. The main advantage of SCA over other methods is its straightforward interpretability; it reveals the network of regions most strongly functionally connected with the seed voxel (or ROI). Furthermore, previous work has shown that functional connectivity measures can be estimated with moderate to high reliability by SCA [30].

While being an attractive approach for many researchers, SCA has some drawbacks that need to be taken into account during analysis and interpretation of the results. Most importantly, strong correlations between the time series of two regions do not imply causal relationship between them, it tells nothing about the exact order of events and causal relationships in the dynamic processing stream. Moreover, the functional connection between two nodes is not necessarily direct (it can be triggered or modulated by a third node).

Since functional MRI enables the measurement of neural activations indirectly through vascular responses, the calculated correlations between BOLD time series are also affected by various neurovascular factors such as the shape and amplitude of the hemodynamic response function. In addition, time series are substantially corrupted by noise of physiological and

hardware-related origin resulting in varying temporal SNR across the brain (see Section 5.3.1). Due to the indirect nature of rs-fMRI and the fact that hemodynamic responses and temporal signal-to-noise ratio are spatially dependent, similarity measures such as correlation coefficient reflect apparent correlations of the underlying neural power fluctuations. Figure 10 illustrates the principle of correlation estimation between BOLD time series and also shows potential confounding factors.

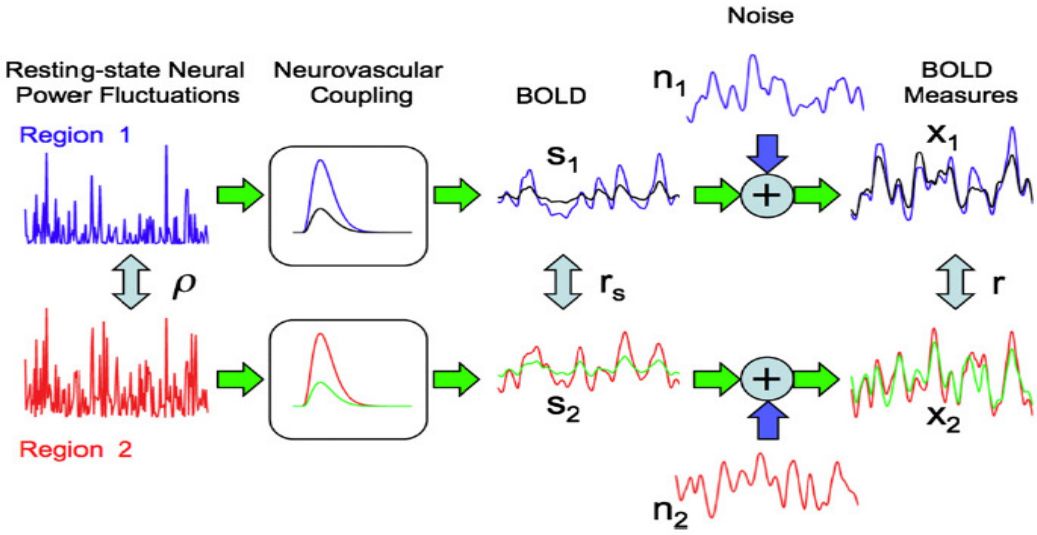

Figure 10. The correlation between the underlying neural fluctuations of two distant regions (blue and red time courses on the left) is denoted by ρ. The measured BOLD time series is modeled by the sum of a BOLD component (s_1 and s_2 for Region 1 and 2, respectively) and a noise component (n_1 and n_2, respectively), where the BOLD component is obtained by convolving the neural power fluctuations with the hemodynamic response function that represents the neurovascular coupling effect. Apparent correlation coefficient r is computed between the measured BOLD signals x_1 and x_2. Note that measured x_1 and x_2 depend on the neurovascular coupling pathway and the level of noise. Different hemodynamic response functions (blue and black curves for Region 1, red and green curves for Region 2) yield different BOLD measures and therefore different apparent correlation coefficients [31].

Another drawback of SCA lies in the a priori assumptions underlying ROI definition. Extracting average time series from inaccurate ROIs that do not match actual functional boundaries can be highly damaging to network estimation [29].

SCA applied to the whole time series implicitly assumes that statistical interdependence of neuronal events is constant throughout the recording period. However, recent papers suggest that dynamic measures (e.g. dynamic correlation obtained from sliding-window analysis) may index changes in macroscopic neural activity patterns and point out that underlying processes may not be statistically stationary [32] [33]. In this thesis I refrain from considering dynamic effects and treat correlations as stationary measures.

4.3 Temporal preprocessing

Resting-state fMRI data contain coherent fluctuations unrelated to neural activity. These noise components originate mainly from physiological artifacts (caused by respiration, cardiac action, residual subject motion etc.) as well as hardware instabilities and magnetic field drifts. Since seed-based connectivity analysis basically involves assessment of temporal similarities in the dataset, coherent signal fluctuations from non-neural processes may result in biased (typically overestimated, see Section 5.4.3) functional connectivity estimation. To obtain unbiased estimates of connectivity, adequate temporal preprocessing is critical.

Several temporal preprocessing strategies (also known as denoising procedures) have been established; the most important ones are the linear-regression based approaches and denoising using independent component analysis. These methods can be used in combination with each other and may also be complemented by other procedures such as filtering in the frequency domain. In this thesis I focused on the linear regression based approaches in order to optimize their usage in terms of sensitivity and specificity of network detection. The following sections describe the basic principles of these preprocessing steps and discuss the methodological and associated interpretative issues.

4.3.1 Filtering

Frequency filtering attempts to isolate frequency components most relevant to the BOLD signal of neural activations. It takes advantage of the fact that noise components may be represented at distinct frequencies from the neural-related signal of interest. For instance, the dominant respiration- and cardiac action related signals are present at around 0.2 and 1 Hz, respectively (for a power spectra of BOLD signals, see 5.3.2). In contrast, BOLD fluctuations that most consistently present resting-state correlations occur within the range of 0.01 to 0.08 Hz [16]. For this reason functional connectivity analysis is typically performed on low-pass filtered datasets retaining frequencies under appr. 0.1 Hz below the usual respiration and cardiac action rates. High-pass filtering is also used in most cases with cut-off frequency below the lowest frequency of interest.

However, a low-pass filter is unable to remove noise components of frequencies higher than the Nyquist frequency (half of the sampling rate) or lower than the low-pass cut-off. Given a typical TR of 2 s (with a Nyquist frequency of 0.25 Hz) as used in this thesis, breath-to-breath respiratory effects are probably filtered out, but cardiac effects and their harmonics, as well as the harmonics of the respiratory noise, are not critically sampled and

can be aliased into the retained frequency range. Additionally, respiration and cardiac rate fluctuate also at low frequencies, further confounding the BOLD signal. Furthermore, residual motion and scanner artifacts are not restricted to a narrow frequency band and spread over the whole spectrum [34]. To achieve critical sampling some studies use fast sampling rates (200-500 ms) at the expense of brain coverage when using conventional BOLD sequences [35]. Another option is to apply additional preprocessing in form of multidimensional linear regression, which allow for removing a number of confounds (see next section).

While resting-state fluctuations are described as low-frequency fluctuations below 0.1 Hz, accumulating evidence suggests that valid and useful neural-related signal is present up to 0.2 Hz, possibly even up to 0.5 Hz [36]. Thus, applying low-pass filter inherently carries the risk of removing useful signal. For this reason some studies refrain from implementing it in the preprocessing pipeline.

4.3.2 Physiological noise regression

As was discussed in the previous chapter, unwanted residual physiological artefacts are still present in the retained frequency range. Physiological noise regression tries to isolate noise components from the fMRI data and incorporate these signals as nuisance regressors in the general linear model [37].

Reasonable regressors for physiological noise can be obtained in several ways. The most straightforward approach is to monitor respiratory and cardiac rates using respiratory belts and pulse oximeters, respectively [38]. Adequate nuisance regressors can be modeled based on these measures that can be used to correct data retrospectively. However, the timing of these physiological signals in the brain is not obvious since they are measured in different parts of the body.

If monitoring devices are not available (as was the case during the measurements done for this thesis), effective estimators of non-neural signal fluctuations need to be derived from the fMRI data. Rigid-body realignment parameters obtained from motion correction (see Fig.9) can serve as such regressors, since it is possible that BOLD signal intensity depends on the spatial location and orientation of the brain (e.g. because of the different position of the voxels from the receiver coil). Differential motion parameters also qualify as nuisance regressors, since movement leads to instant changes in the signal intensity due to spin-history effect and perturbation of the magnetic field, which may be modeled as a linear change in the signal intensity. Additional commonly used regressors include average signal of the cerebral white matter (WM) and the ventricles containing cerebrospinal fluid (CSF). The mean WM

and CSF time series are calculated by averaging signal over all voxels within a WM or CSF mask for each time point. Regression of signals from WM and CSF is motivated by the fact that these regions contain a relatively high proportion of noise caused by the cardiac and respiratory cycles [39] and they do not reflect neural fluctuations. It is further assumed that motion-related as well as physiological effects cause the same pattern of activity over time in the gray-matter ROIs (although not necessarily at the same magnitude) [40]. Eventually, successful estimation and correction for these non-neural noise sources allow for the exclusion such confounding effects from the analysis. Regression of the global signal (the average signal over all voxels of the brain) has also been proposed for artifact reduction [41], but it presents challenging interpretative issues discussed in detail in Section 4.3.3.

Generally, the acquired fMRI time series are analyzed within the framework of general linear model (GLM). This statistical linear model assumes that the time series of a voxel can be written as:

$$\underline{\boldsymbol{Y}} = \underline{\underline{\boldsymbol{X}}} \cdot \underline{\boldsymbol{\beta}} + \underline{\boldsymbol{e}} \tag{25}$$

with the measured time series $\underline{\boldsymbol{Y}}$, the design matrix $\underline{\underline{\boldsymbol{X}}}$ containing all regressors (also known as predictors or explanatory variables) in its columns, the vector of parameter estimates $\underline{\boldsymbol{\beta}}$ and the residuals $\underline{\boldsymbol{e}}$. The errors are assumed to follow a multivariate normal distribution. The case of a single regressor is called simple linear regression. In contrast, multiple linear regression (multidimensional linear regression) refers to the case when multiple regressors are incorporated in the model, which is typical for SCA preprocessing.

This model thus assumes that the relation between the observed time series $\underline{\boldsymbol{Y}}$ and the columns of the design matrix $\underline{\underline{\boldsymbol{X}}}$ (regressors) is linear with the scaling factors $\underline{\boldsymbol{\beta}}$ and with an unobserved $\underline{\boldsymbol{e}}$ random variable adding noise to the linear model. Our goal in SCA preprocessing is to best model the linear contributions of physiological and non-physiological noise in the fMRI time series by incorporating regressors expected to reflect noise (motion parameters, WM/CSF signal etc.) in the design matrix. This "best modeling" is usually defined in terms of yielding the smallest least squares of the error. Since the term $\underline{\boldsymbol{Y}}$ is observed and $\underline{\underline{\boldsymbol{X}}}$ is predetermined, this is achieved by finding the $\underline{\boldsymbol{\beta}}$ vector that minimizes the sum of squares of the error term $\underline{\boldsymbol{e}}$. This procedure is also called "fitting the model" and can be mathematically expressed as:

$$\underline{\boldsymbol{e}}\,\underline{\boldsymbol{e}}^{\boldsymbol{T}} = \left(\underline{\boldsymbol{Y}} - \underline{\underline{\boldsymbol{X}}} \cdot \underline{\boldsymbol{\beta}}\right)\left(\underline{\boldsymbol{Y}} - \underline{\underline{\boldsymbol{X}}} \cdot \underline{\boldsymbol{\beta}}\right)^{T} = \left(\underline{\boldsymbol{Y}} - \underline{\widehat{\boldsymbol{Y}}}\right)\left(\underline{\boldsymbol{Y}} - \underline{\widehat{\boldsymbol{Y}}}\right)^{T} \rightarrow \min \tag{26}$$

The term $\underline{\underline{e}}\,\underline{\underline{e}}^{T}$ is the vector notation for the sum of squares. The optimal $\underline{\underline{\beta}}$ weights using the ordinary least squares approach are obtained non-iteratively by the following equation:

$$\underline{\underline{\beta}} = \left(\underline{\underline{X}}^{T}\underline{\underline{X}}\right)^{-1}\underline{\underline{X}}^{T}\underline{\underline{Y}} \tag{27}$$

provided that $\left(\underline{\underline{X}}^{T}\underline{\underline{X}}\right)^{-1}$ exists. After determining the optimal $\underline{\underline{\hat{\beta}}}$ weights the corrected data set can be calculated as:

$$\underline{\underline{Y}}_{corr} = \underline{\underline{Y}} - \underline{\underline{X}} \cdot \underline{\underline{\hat{\beta}}} \tag{28}$$

Multiple linear regression is performed on a voxel-by-voxel basis and the resulting $\underline{\underline{Y}}_{corr}$ corrected data sets will be used to compute cross-correlations for assessing functional relations between voxels or ROIs.

4.3.3 Regression of global signal

Global signal regression is a preprocessing technique in which the mean global signal is used as a temporal covariate and regressed out using linear regression. Is has been shown that regression of the global signal is beneficial for improving the predictive power of correlation measures and improve the specificity of functional connectivity analysis [42].

However, the validity of global signal regression has recently come under debate because it has the ability to introduce artifactual negative correlations between brain regions. Since the global signal contains all resting-state signal changes as well as all sources of noise including physiological and non-physiological effects, its regression can reduce non-neural signal correlations to a greater extent. Windischberger et al. [43] demonstrated with a simple example that truly negatively correlated (anticorrelated) signals remain to be anticorrelated after global signal correction, whereas uncorrelated signals are shifted towards negative correlation coefficients. According to Murphy et al. [44], voxel correlation analysis of global signal corrected data sets always finds negative correlations regardless of the seed voxel chosen. Based on these studies, there is a significant risk of introducing anticorrelations by global signal regression.

The primary difficulty of global signal regression is that the extent to which the whole-brain signal represents neurophysiological signal or noise is generally not known. It is also unclear how the whole-brain signal correlates with signals of true neurophysiological origin. However, the whole-brain signal at rest has been found to correlate with the breath-to-breath variation in the end-tidal partial pressure of carbon dioxide [45].

The fact that global signal regression forces the existence of negative correlations by centering the correlation coefficients around zero may have important implications regarding the validity of large anticorrelated networks discussed in Section 5.4.3. The emergence of such networks after performing global signal regression can have multiple reasons. It is possible that anticorrelated brain regions are simply the result of shifting the correlation histogram to be centered around zero. On the other hand, neurophysiologically meaningful negative correlations may only become detectable after the removal of nonspecific noise correlations. Knowing the exact origin of anticorrelations is critically important, however, at present there is no general agreement on this issue [18][43]. Based on these considerations it seems obvious that anticorrelations should be approached with caution.

Despite the concerns raised about the validity of global signal regression it is still a common and useful processing technique in some situations. However, alternate methods have recently been developed to circumvent the potential issues with global signal regression. Of particular importance is the anatomical component based noise correction (aCompCor) denoising procedure, which has been shown to produce similarly robust anticorrelated networks without the inclusion of global signal regression [46].

4.3.4 Anatomical component based noise correction method

The concept of "noise region of interest" has already been introduced in Section 4.3.2. Noise ROIs are regions such as white matter and cerebrospinal fluid, in which fMRI signal is not expected to reflect any neural activity, thus representing primarily physiological noise. Based on the assumption that signal from noise ROIs can be used to accurately model physiological fluctuations in gray matter regions, it is a common practice to regress out mean signal from each of these noise ROIs in order to reduce non-specific correlations. The novel anatomical component based noise correction (aCompCor) approach extends this idea by extracting multiple signals from these areas using the technique of principal component analysis [47]. In comparison to the mean signal from noise regions, signals captured by principal components derived from these noise ROIs serve as a richer representation of the underlying physiological noise and can better account for voxel-specific phase differences in physiological noise due to the potential of principle component analysis to identify temporal pattern of physiological noise. The main advantage of the aCompCor approach is its ability to significantly reduce noise in the fMRI dataset without the inclusion of potential signals of neural origin [46].

The first step of applying aCompCor is the determination of noise ROIs from which principal components will be extracted. Posterior probability maps created during

segmentation of the anatomical image (see Section 4.1.4) are used to identify voxels that consist primarily of either WM or CSF. Each of the probability masks is thresholded (usually at $p > 0.5$) to exclude voxels that most probably consist of other type of tissue. Subsequent erosion of the masks is also used sometimes to minimize partial volume effects. Figure 11 illustrates thresholded and eroded WM and CSF probability masks with the red areas showing the voxels that survive one-voxel erosion. Subsequently, fMRI timeseries in the functional volumes are extracted within the resulting masks. Since spatial smoothing blurs the boundaries of different tissue types, it is important to extract fMRI signal for each noise region from the unsmoothed dataset. An alternative method of defining noise regions is to include voxels with the lowest tSNR (usually referred to as "tCompCor") values based on the assumption that they can suitably characterize physiological noise, but this approach is less commonly used and will not be tested in the thesis.

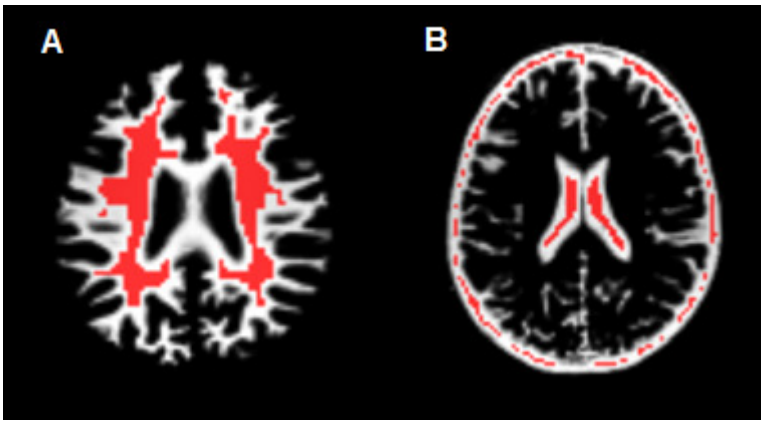

Figure 11. A: White matter mask created by one-voxel eroding the thresholded ($p > 0.5$) WM probability map (red area), overlaid on the WM probability map (grey area). B: CSF probability map in grey, thresholded and eroded mask in red.

Principal component analysis (PCA) is a statistical procedure that converts a set of observations (variables) with possible redundancies to a set of linearly uncorrelated variables using orthogonal transformation. It thus involves a "re-expression" of the original dataset in a way that the resulting data possess some useful properties. The re-expressed variables are called principal components and their number is less than or equal to the original observations.

Suppose we have m observations (row vectors) contained in matrix $\underline{\underline{\boldsymbol{X}}}$:

$$\underline{\underline{\boldsymbol{X}}} = \begin{bmatrix} \underline{\boldsymbol{x}}_1 \\ \vdots \\ \underline{\boldsymbol{x}}_m \end{bmatrix}$$

This expression of the data may not be optimal as there can be correlations among the observations leading to redundancies in the dataset. The covariance matrix $\underline{\underline{\boldsymbol{S}}}_x$ quantifies all dependencies between pairs of observations[9]:

$$\underline{\underline{\boldsymbol{S}}}_x = \frac{1}{n-1}\underline{\underline{\boldsymbol{X}}}\,\underline{\underline{\boldsymbol{X}}}^T \tag{29}$$

$\underline{\underline{\boldsymbol{S}}}_x$ is an m x m symmetric matrix where the ij^{th} element is the variance or covariance between $\underline{\boldsymbol{x_i}}$ and $\underline{\boldsymbol{x_j}}$. The diagonal terms of $\underline{\underline{\boldsymbol{S}}}_x$ are the variances of the observations, while the off-diagonal terms are the covariances between observations.

Principal component analysis tries to eliminate covariances among observations by changing the basis of expression of the original dataset. Let $\underline{\underline{\boldsymbol{P}}}$ be the orthonormal matrix associated with the change of basis that performs a linear transformation on data matrix $\underline{\underline{\boldsymbol{X}}}$:

$$\underline{\underline{\boldsymbol{Y}}} = \underline{\underline{\boldsymbol{P}}}\,\underline{\underline{\boldsymbol{X}}} \tag{30}$$

where $\underline{\underline{\boldsymbol{Y}}}$ is the matrix of observables expressed with the new basis vectors. The covariance matrix of the re-expressed data is

$$\underline{\underline{\boldsymbol{S}}}_y = \frac{1}{n-1}\underline{\underline{\boldsymbol{Y}}}\,\underline{\underline{\boldsymbol{Y}}}^T \tag{31}$$

The goal of PCA is to find $\underline{\underline{\boldsymbol{P}}}$ such that $\underline{\underline{\boldsymbol{S}}}_y$ is diagonalized corresponding to zero covariances among observations. Let us rewrite $\underline{\underline{\boldsymbol{S}}}_y$ in terms of the selection of $\underline{\underline{\boldsymbol{P}}}$:

$$\underline{\underline{\boldsymbol{S}}}_y = \frac{1}{n-1}\underline{\underline{\boldsymbol{Y}}}\,\underline{\underline{\boldsymbol{Y}}}^T = \frac{1}{n-1}\left(\underline{\underline{\boldsymbol{P}}}\,\underline{\underline{\boldsymbol{X}}}\right)\left(\underline{\underline{\boldsymbol{P}}}\,\underline{\underline{\boldsymbol{X}}}\right)^{\boldsymbol{T}} = \frac{1}{n-1}\underline{\underline{\boldsymbol{P}}}\,\left(\underline{\underline{\boldsymbol{X}}}\,\underline{\underline{\boldsymbol{X}}}^{\boldsymbol{T}}\right)\underline{\underline{\boldsymbol{P}}}^{\boldsymbol{T}} = \frac{1}{n-1}\underline{\underline{\boldsymbol{P}}}\,\underline{\underline{\boldsymbol{A}}}\,\underline{\underline{\boldsymbol{P}}}^{\boldsymbol{T}} \tag{32}$$

where $\underline{\underline{\boldsymbol{A}}} = \underline{\underline{\boldsymbol{X}}}\,\underline{\underline{\boldsymbol{X}}}^{\boldsymbol{T}}$ is an m x m symmetric matrix. PCA takes advantage of the fact that a symmetric matrix can be diagonalized by a matrix of its orthonormal eigenvectors. Furthermore, by selecting $\underline{\underline{\boldsymbol{P}}}$ to be the a matrix where each row is an eigenvector of $\underline{\underline{\boldsymbol{X}}}\,\underline{\underline{\boldsymbol{X}}}^{\boldsymbol{T}}$, $\underline{\underline{\boldsymbol{A}}}$ can be decomposed as $\underline{\underline{\boldsymbol{A}}} = \underline{\underline{\boldsymbol{P}}}^{\boldsymbol{T}}\underline{\underline{\boldsymbol{D}}}\,\underline{\underline{\boldsymbol{P}}}$, where $\underline{\underline{\boldsymbol{D}}}$ is a diagonal matrix and $\underline{\underline{\boldsymbol{P}}}^{\boldsymbol{T}}$ is the matrix of eigenvectors of $\underline{\underline{\boldsymbol{A}}}$ arranged as columns. Further evaluation of $\underline{\underline{\boldsymbol{S}}}_y$ yields:

$$\underline{\underline{\boldsymbol{S}}}_y = \frac{1}{n-1}\underline{\underline{\boldsymbol{P}}}\,\underline{\underline{\boldsymbol{A}}}\,\underline{\underline{\boldsymbol{P}}}^{\boldsymbol{T}} = \frac{1}{n-1}\left(\underline{\underline{\boldsymbol{P}}}\,\underline{\underline{\boldsymbol{P}}}^{\boldsymbol{T}}\right)\underline{\underline{\boldsymbol{D}}}\,\left(\underline{\underline{\boldsymbol{P}}}\,\underline{\underline{\boldsymbol{P}}}^{\boldsymbol{T}}\right) = \frac{1}{n-1}\left(\underline{\underline{\boldsymbol{P}}}\,\underline{\underline{\boldsymbol{P}}}^{-\boldsymbol{1}}\right)\underline{\underline{\boldsymbol{D}}}\,\left(\underline{\underline{\boldsymbol{P}}}\,\underline{\underline{\boldsymbol{P}}}^{-\boldsymbol{1}}\right) = \frac{1}{n-1}\,\underline{\underline{\boldsymbol{D}}} \tag{33}$$

[9] The normalization factor $\frac{1}{n-1}$ is used instead of the simple $\frac{1}{n}$ factor in order to provide unbiased estimator for the covariance.

where I used the fact that the transpose of an orthogonal matrix is its inverse. It is evident from this result that choosing $\underline{\underline{\boldsymbol{P}}}$ to contain the eigenvectors of $\underline{\underline{\boldsymbol{X}}}\,\underline{\underline{\boldsymbol{X}}}^{\boldsymbol{T}}$ in its rows diagonalizes $\underline{\underline{\boldsymbol{S}}}_{\boldsymbol{y}}$. After applying this $\underline{\underline{\boldsymbol{P}}}$, the rows of $\underline{\underline{\boldsymbol{Y}}}$ will become the principal components. The principal components are arranged in such a way that the first principal component has the largest variance and subsequent components possess decreasing variance always under the constraint that they are uncorrelated with the preceding components.

5. Optimization of preprocessing strategy in resting-state data

5.1 Subjects

Thirty-two healthy participants (mean age: 25.3 ± 5.3, 20 males) were included in the study, which was approved by the Ethics committee of the Semmelweis University. Participants were clinically normal young adults without a history of neurological or psychiatric illness, and not taking any psychoactive medications. Signed informed consent was obtained prior to participation. Two subjects were excluded from all of the subsequent analysis due to extensive head motion during scanning (see Section 5.6.3).

5.2 Methods

All data were collected on a 3T Philips Achieva scanner located at MR Research Center of Semmelweis University and equipped with an 8 channel SENSE head coil supplied by the vendor. The functional imaging data were acquired using a gradient echo echo-planar imaging (EPI) sequence sensitive to blood oxygenation level-dependent (BOLD) contrast with the following parameters: 36 contiguous axial slices of 4 mm thickness aligned parallel to the line connecting the anterior and posterior commissure and perpendicular to the median sagittal plane providing whole brain coverage, TR: 2000 ms, TE: 30 ms, matrix size: 80 x 80, voxel size: 3 x 3 x 4 mm, flip angle: 70°, slice order: ascending. Each BOLD run consisted of 260 volumes, making the total acquisition time nearly 9 minutes. Additionally, a high-resolution isotropic T1-weighted Turbo Spin Echo (TSE) structural image was obtained for each subject.

Subjects were instructed to simply rest in the scanner and not to fall asleep. The scanner room was darkened. Earplugs were used to attenuate scanner noise and head motion was restrained with a foam pillow. We adopted an eyes-open approach because a previous fMRI study indicates that resting with eyes open results in more robust estimates of functional connectivity within the default mode network and dorsal attention system [18] and we also wanted to minimize the risk of subjects falling asleep.

A series of preprocessing steps was conducted that are common to most fMRI analyses. Spatial preprocessing was performed using SPM8. The first four volumes of each run were discarded by the scanner as dummy acquisitions to allow for T1-equilibration effects. Slice acquisition dependent time shifts were corrected on a volume-by-volume basis. 6-parameter rigid body translation and rotation from each volume to the first volume were used to correct for head motion. Then, the high-resolution anatomical image was coregistered

to the mean functional image. Normalization was achieved by computing affine and non-linear transforms connecting the T1-weighted anatomical image with a T1 template in the Montreal Neurological Institute (MNI152) atlas space [48]. In the same step, segmented probability maps were also created both in the native space and in the normalized stereotactic space. Data were resampled to 2-mm isotropic voxels and spatially smoothed using a 4 mm FWHM Gaussian kernel. Each dataset was masked using the freely available MNI brainmask[10] bundled with SPM to eliminate extracerebral tissues from the further analysis.

5.3 Signal and noise in the data

In this section I analyzed some properties of the acquired dataset: its temporal signal-to-noise ratio and power spectrum. These characteristics can help better understand the effect of multiple noise sources on the data and therefore serve as guides for establishing an optimal preprocessing strategy.

5.3.1 Temporal signal-to-noise ratio

While spatial SNR is used to quantitatively describe the quality of anatomical MR images, tSNR has proved to be a useful measure of image time course stability in fMRI images. tSNR depends on hardware related factors (field strength, coil quality, quality of shimming etc.), data acquisition parameters (type of pulse sequence, slice thickness, voxel size etc.) and physiological noise. In particular, tSNR has been found to be a good predictor of the extent to which physiological noise corrupts resting-state datasets [49]. As will be seen in Section 5.6.1, tSNR can be used to identify subjects with high level of head motion. A good signal quality with high tSNR is particularly important for seed-based correlation analysis, since correlation values can be seriously affected by low tSNR values across the brain.

It is expected that different parts of the brain are more susceptible to physiological noise and other data instabilities. In order to assess this spatial dependency, temporal SNR was calculated on a voxel-by-voxel basis from the unsmoothed dataset. Masks created by thresholding the segmentation probability maps at 50% were used to extract signals from the GM, WM and CSF to assess the tissue-specific differences in the tSNR. Voxel-wise tSNR was averaged within each tissue mask. The tissue-specific mean tSNR with its associated standard deviation across the 30 subjects was found to be the following: $\mathbf{85.30 \pm 45.33}$ for GM, $\mathbf{129.46 \pm 65.47}$ for WM and $\mathbf{48.81 \pm 23.79}$ for CSF. These results are consistent

[10] Applied template: SPM apriori binary brain mask available at: spm/apriori/brainmask.nii.

with other studies [50] and suggest that cerebrospinal fluid is the most sensitive tissue to physiological noise followed by grey and white matter. Extracted signals from WM and particularly from CSF can thus be a good estimator of physiological variations during the regression of nuisance variables.

Figure 12A displays a slice of the voxel-by-voxel tSNR map averaged across subjects, using the imaging capabilities of MRIcroN[11]. Note that tSNR variations closely resemble anatomical structures with the ventricles and edges of the brain having the lowest values. Color-coded tSNR values projected onto the surface of the standard brain template[12] of MRIcroN are also depicted in Fig.12B, using the 3D visualization of MRIcroGL[13]. tSNR is generally lower at the cortical surface but there are regions with particularly low signal quality including orbitofrontal cortex or inferior temporal lobe. These signal instabilities are caused by the high magnetic susceptibility differences between these areas and neighboring air-filled cavities (ear canal, nasal cavities). On the other hand, some regions (particularly the inferior parietal lobe) exhibit excellent tSNR.

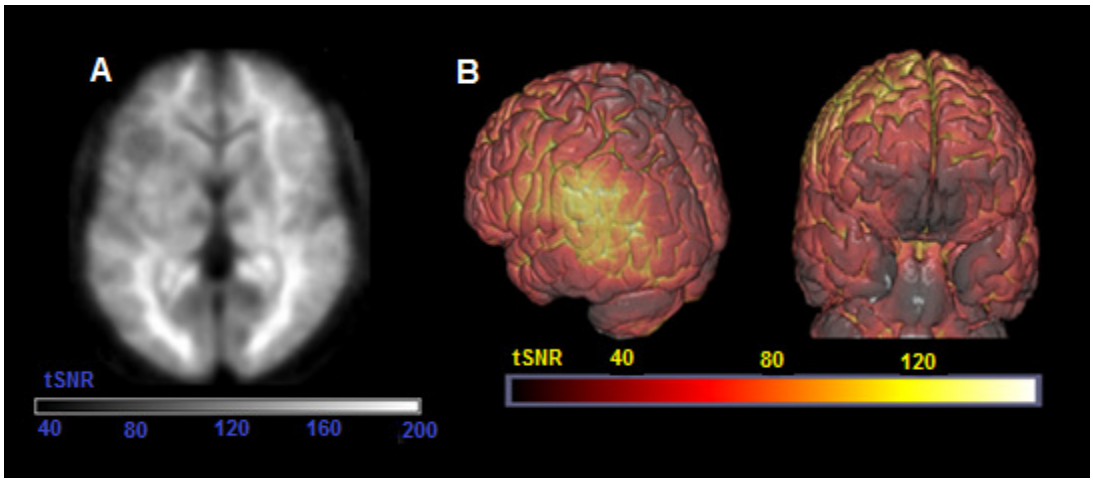

Figure 12. A: Grayscale map of tSNR averaged across subjects (slice MNI coordinate: z=6). B: Color-coded surface projections of the average tSNR map.

5.3.2 Power Spectrum

Power spectrum (power spectral density) is a mathematical tool that allows us to obtain the portion of a discrete signal's power falling within a given frequency bin. Peaks in the spectrum indicate dominant signal components. In this section I analyzed the frequency spectra of BOLD time series in an attempt to test the hypothesis that resting-state BOLD

[11] MRIcroN Software of McCausland Center For Brain Imaging: http://www.mccauslandcenter.sc.edu/mricro/mricron/install.html
[12] Applied template: ch2.better.nii.gz
[13] MRIcroGL software of the same insitute as in [9]: http://www.mccauslandcenter.sc.edu/mricrogl/

signals are primarily low-frequency fluctuations and to identify signal components unlikely to be modulated by neural activity.

The same tissue masks as applied in Section 5.3.1 were used to extract tissue-specific voxel time series from the unsmoothed dataset. Power spectrum of each voxel's time series was computed using the Fast Fourier Transform (FFT) implementation of Matlab[14]. Given the temporal resolution of $2\ s$ and the 260 data points, the Nyquist frequency was $0.25\ Hz$ with a frequency resolution of $0.00192\ Hz$. Power spectra within each tissue type and across subjects were averaged and plotted on log-log scale in Figures 13A,B,C. Furthermore, the time series corresponding to GM voxels underwent temporal preprocessing and the resulting mean power spectrum was also plotted in Fig.13D.

The group-level average power spectra were found to be similar in each tissue type. In general, the power decreases with increasing frequency, however, an increase in power is observed around $0.2\ Hz$ with peak value at $0.2385\ Hz$. This peak reflects the respiratory-induced breath-to-breath signal variations corresponding to a typical period of 4-5 s. Noise sources of higher frequencies cannot be critically sampled and are therefore aliased towards the low-frequency bands. Individual power spectra of some subjects also exhibit significant peaks at $0.1\ Hz$, which has been shown to be a characteristic frequency of vasomotor action that cause arterial blood pressure to fluctuate rhythmically [51] but this peak is not observable in the group level. Also note that the highest power in CSF spectrum compared to other tissues is a direct consequence of the higher fluctuations associated with a lower tSNR (see Section 5.3.1).

Zarahn et al. fitted the BOLD power spectrum with a power-law expression and found a $1/f$ behavior with respect to the frequency [52]. In numerous other studies, BOLD signals are consistently referred to as "low-frequency" or "$1/f$" signal. The obtained spectra seem to corroborate this power-law behavior, since power values appear as straight lines up to a certain limit. Power law functions of the form a/f^b were fitted to the individual spectra restricted to the interval of $0 - 0.15\ Hz$ and following b values (negative slope) were found: $\mathbf{0.9038 \pm 0.1746}$ for GM, $\mathbf{0.7374 \pm 0.2150}$ for WM and $\mathbf{0.7060 \pm 0.1475}$ for CSF. In fact, these negative slope values suggest an approximate $1/f$ behavior. Interestingly, the power spectra of the signals from WM and CSF also decreases according to power law implying that power law behavior is an intrinsic characteristic of the BOLD signal irrespective of the tissue type. The slope of GM power spectrum and therefore the fraction of

[14] MATLAB 6.1, The MathWorks Inc., Natick, MA, 2000.

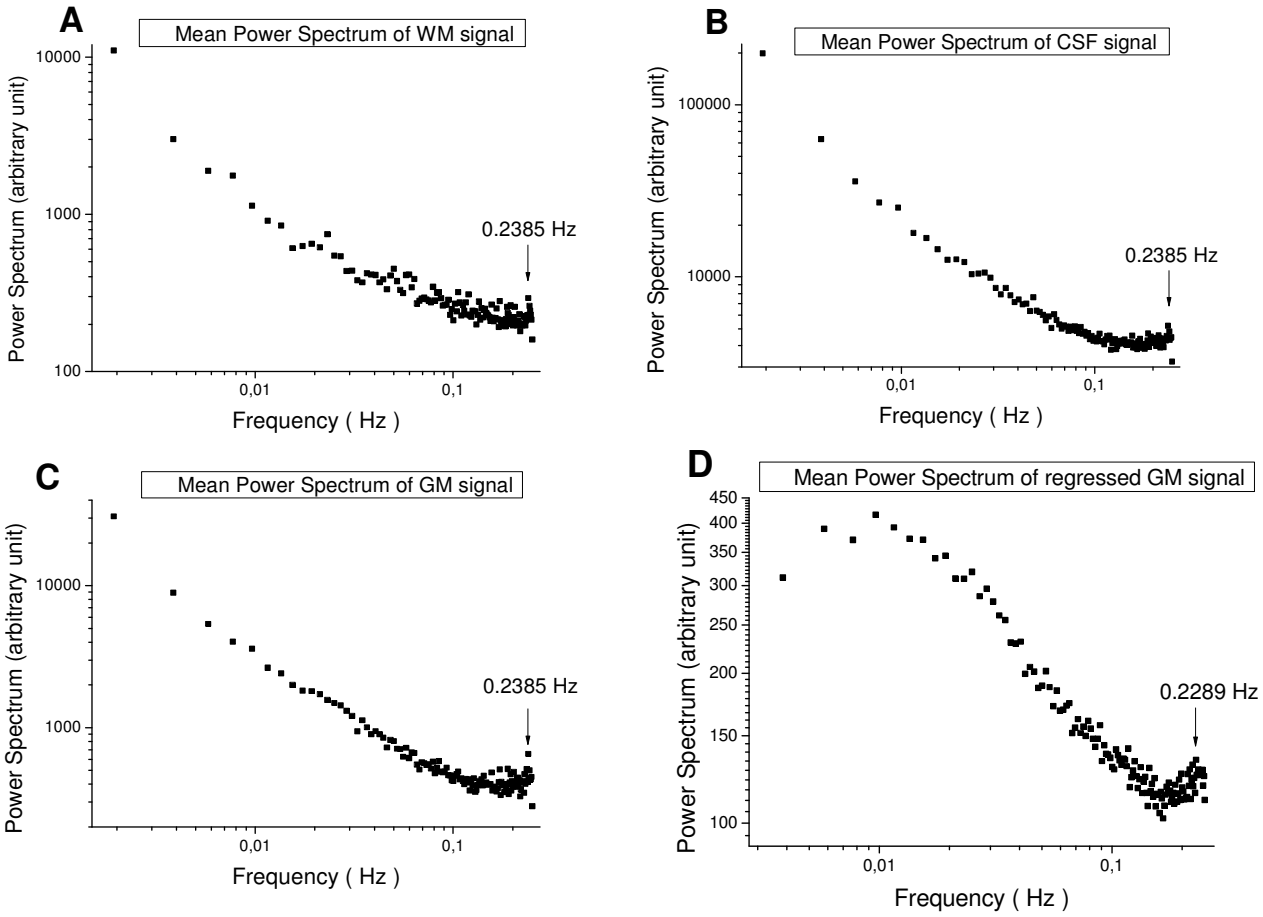

Figure 13. A: Group-level average power spectrum of voxel time courses within the white matter mask. B: Group-level average power spectrum within CSF mask. C: Group-level average power spectrum within grey matter mask. In A,B,C, voxel time courses were not temporally preprocessed. D: Group-level average power spectrum of temporally preprocessed time courses within GM mask. Note the presence of a peak between 0.2 and 0.25 Hz in all figures.

low frequencies are higher than those of the other tissues, which may be caused by the hemodynamics that act as a low-pass filter. However, the extent to which hemodynamic response function affect the power spectrum is generally not known.

I also tested whether regression of signals from noise ROIs is able to remove the respiratory-induced peak at $0.2\ Hz$ and higher. Five principal components from the WM and CSF masks, motion parameters as well as a linear trend (for details, see Section 5.4.2) were regressed out voxel-wise. The peak is still present in the power spectrum of the denoised data (Fig.13D) suggesting that linear regression of noise estimator signals alone is not enough to eliminate all non-neural components. Furthermore, the power of frequencies below $0.01\ Hz$ is highly decreased due to linear detrending. To restrict correlation analysis to a frequency band dominated by neural activity induced fluctuations, a frequency band bass filter with low and

high cut-off frequencies was created. The lower limit of the band was chosen to be $0.01\ Hz$, because frequencies below are primarily resulted from the linear trend of the signal. The higher cut-off frequency is harder to determine as neural related fluctuations do not cease at a single frequency. However, an upper limit of $0.1\ Hz$ appears to be a good compromise with respect to the high power of noise above this frequency. Using similar considerations, most studies apply a low-frequency cut-off of around $0.008 - 0.1\ Hz$, and a high-frequency cut-off between $0.08 - 0.15\ Hz$ [18][43][46].

5.4 Influence of temporal preprocessing steps on connectivity measures

In this section I applied several multidimensional linear regression approaches to remove artificial coherencies in the resting-state data from 30 subjects. Section 5.4.1 introduces the definition of reference ROIs, while detailed description of temporal processing steps are discussed in Section 5.4.2. I examined the impact of preprocessing steps on sensitivity and specificity of functional connectivity measures in Section 5.4.3 to provide recommendations for optimization.

5.4.1 Region of interest definition

In order to run a performance comparison between different preprocessing approaches, several quantitative metrics need to be defined that can be used to assess improvements or degradations in functional connectivity measures. Similar to the approach in [18] and [43], a set of a priori defined networks were chosen to construct metrics that represent either estimates of true neural correlations (signal metrics) or an estimate of non-neural correlation (noise metric). The two "signal networks" selected to create signal metrics were the **default mode network** (DMN) and the **dorsal attention system** [1]. Each of these well-known networks has multiple nodes with strong correlations among them. The two signal metrics were defined as the mean correlation coefficients among the nodes within each of these networks. Noise metric was estimated as the mean correlation coefficient among a reference set of regions including **primary motor**, **visual** and **auditory cortex**, among which no correlation is expected, since they are part of independent functional systems [53]. Note that in contrast to the signal metrics, the noise metric represents an averaged between-network coefficient. Furthermore, since default mode network is a task-negative and dorsal attention system is a task-positive system, the mean value of the pairwise between-network correlations among the nodes of these networks can serve as an anticorrelation signal metric. Throughout

the following sections, these metrics were used as a means to assess signal and noise for all the subsequent processing strategies.

Identification of nodes within each of these networks were performed as follows. As a seed region, posterior cingulate cortex (PCC) was selected, because it has been found to be a major hub in the default mode network [54]. The MNI coordinates of this PCC seed were (0, -53, 26) based on previous studies and the generated seed ROI had a radius of 10 mm [18]. A correlation map for each subject was created by computing correlation coefficients between the mean time series within the PCC seed and the time courses of all acquired voxels within the brain mask. Subsequently, group level map was obtained by averaging individual correlation maps across subjects. While the arbitrary selection of the PCC coordinates may have influences on the individual correlation maps, significant differences using slightly other seeds is not expected on the group level. Centers of well-established nodes of the DMN including left lateral parietal cortex (LLP), right lateral parietal cortex (RLP) and medial prefrontal cortex (MPFC) were identified based on the locations of voxels whose time courses had the highest correlations with the signal of the PCC seed region. Furthermore, being a central node in the network, PCC was expected to be negatively correlated with regions of the dorsal attention system including bilateral frontal eye field (FEF), bilateral intraparietal cortex (IPS) and bilateral middle temporal area (MT). The centers of these nodes were defined as the voxels whose time courses have the highest negative correlations with the reference time course of PCC seed. In the cases of primary motor, auditory and visual networks I relied on previous studies in determining the centers of these regions [18].

Finally, seed regions corresponding to each node were defined as all voxels within the 10 mm radius of the previously obtained seed centers. Fig.14A illustrates the schematic locations of seed regions corresponding to the default mode network, dorsal attention system and reference networks. Fig.14B displays the way DMN was defined: peak voxels corresponding to its nodes were identified on the group level correlation map. Before computing correlation values, the data underwent a regression of 5 principal components specified in Section 5.4.2. Note that Fig.14B shows the peak voxels only schematically, because real peak voxels are in different slices of the image. The exact centers of the seed regions in MNI coordinates are listed in Table 1.

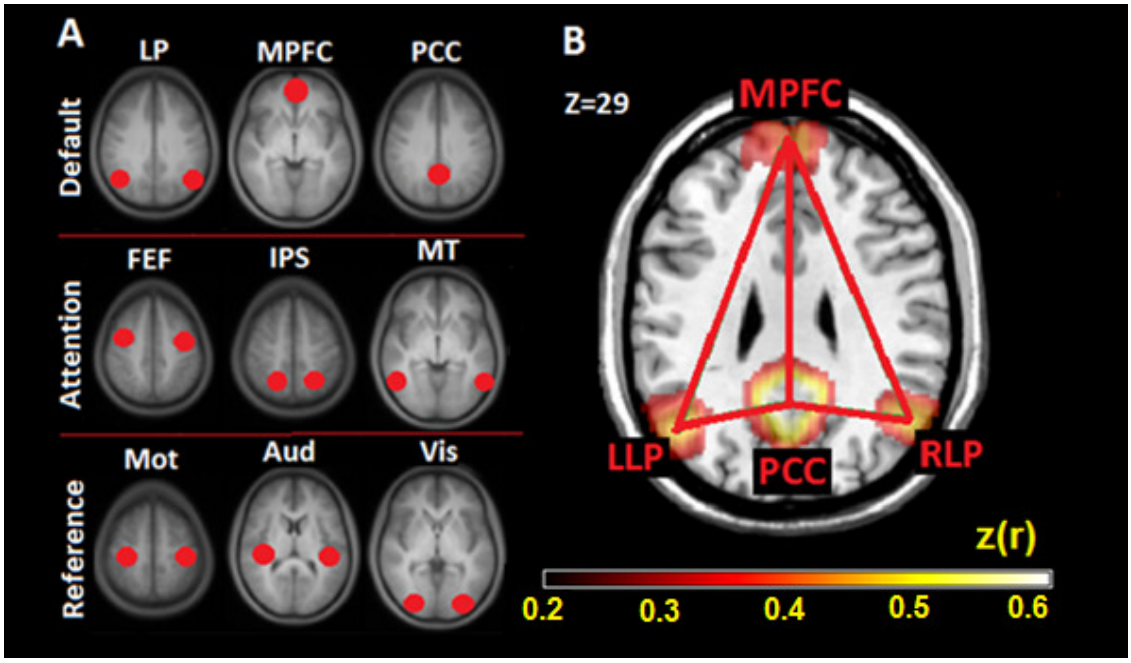

Figure 14. A: Schematic locations of seed regions in the default mode network, dorsal attention system and in the reference networks including motor, auditory and visual network. The exact locations are contained in Table 1. B: Illustration of the node identification procedure. Group-level z correlation map is created with PCC seed region, and peak voxels are considered as nodes of the DMN network (LLP, RLP, PCC, MPFC). Note that peak voxels are schematically displayed in this figure, because real peak values are in different slices of the correlation map.

Table 1. The centers of ROIs are listed with their abbreviation, laterality and MNI coordinates.

Area	Abbreviation	L/R	MNI coordinates		
			X	Y	Z
Posterior Cingulate Cortex	PCC	medialis (med)	0	-53	26
Lateral parietal cortex	LP	L	-48	-66	32
		R	52	-60	28
Medial prefrontal cortex	MPFC	med	2	62	4
Frontal eye field	FEF	L	-26	-2	58
		R	30	2	58
Intraparietal cortex	IPS	L	-40	-44	44
		R	36	-44	44
Middle temporal area	MT	L	-54	-58	-6
		R	56	-54	-4
Motor cortex	Mot	L	-36	-25	57
		R	36	-25	57
Auditory cortex	Aud	L	-43	-26	12
		R	43	-25	57
Visual cortex	Vis	L	-30	-88	0
		R	30	-88	0

5.4.2 Temporal processing steps

Once the networks with corresponding nodes and the different metrics have been defined, the impact of various temporal preprocessing steps on the correlation strengths within and among the seed regions of these networks can be explored. I performed a variety of preprocessing strategies on the acquired resting-state dataset to systematically assess whether the given procedure maximized the correlation strengths within the signal networks and minimized them within the reference networks. After preprocessing, the mean signal was extracted from each of the ROIs of 10 mm radius listed in Table 1, and correlations within and between the specified networks were calculated to construct signal and noise metrics.

Ten (#0 - #9) different preprocessing strategies were tested and compared in the analysis. The details of each preprocessing strategy with the factors for which the data have been corrected are given in Table 2. Although these procedures were covered in Section 4.3, some methodological issues and data specific details were not discussed there.

First, all of the preprocessing strategies were prepended by the spatial preprocessing procedures specified in Section 5.2, with the exception of the #0 strategy, where spatial smoothing was left out to explicitly analyze the correlations in the unsmoothed dataset. Second, voxel time courses were intensity-normalized to compensate for the substantial intensity differences between voxel time series caused by physical and physiological aspects of MRI scanning. However, this step is less of an importance in seed correlation analysis, because both GLM framework and the formula of correlation coefficient are not affected by the level of signal. The percent signal change was used for normalization that transforms each intensity value X_i according to $X_i' = \left(\frac{X_i - \bar{X}}{\bar{X}}\right) \cdot 100$, where X_i' denotes the transformed intensity value, and $\bar{X}$ the voxel's mean time course.

Table 2. Details of the preprocessing strategies. + refers to the application of the particular procedure.

Preprocessing approach	#0	#1	#2	#3	#4	#5	#6	#7	#8	#9
smoothing	-	+	+	+	+	+	+	+	+	+
frequency band-pass filtering	-	-	+	+	+	+	+	+	+	+
regression of motion parameters	-	-	-	+	+	+	+	+	+	+
regression of mean WM, CSF signal	-	-	-	-	+	-	-	-	-	+
regression of global signal	-	-	-	-	-	-	-	-	-	+
number of regressed principal comp.	0	0	0	0	0	3	5	10	15	0

Principal component analysis of the extracted signal from the noise ROIs and multiple linear regression was performed using the CONN toolbox[15] that runs under Matlab environment. Correlation maps created by this software were plotted by MRIcron. All regression procedures and band-pass filtering were performed voxel-wise.

Noise ROIs were created from the tissue probability maps thresholded at $p > 0.5$ and subsequently one-voxel eroded (see Fig.11) to avoid partial volume effects. Interestingly, the one-voxel erosion of the CSF restricts the noise ROI of CSF by far more than in the case of WM. While on average $(\mathbf{27.41 \pm 1.56})\%$ of the voxels for the WM survive the one-voxel erosion, this value is only $(\mathbf{7.54 \pm 4.78})\%$ for the CSF. This is due to the fact that cerebrospinal fluid is distributed in thinner anatomical structures particularly around the cortical surface. These masks were applied to the unsmoothed dataset to extract mean signals as well as principal components.

In order to minimize redundancies in the GLM model, CONN regresses out motion parameters (6 rigid-body motion parameters + backward derivatives) from the BOLD time series within WM and CSF masks before PCA decomposition is applied. This approach avoids that the same subspace is spanned by additional components generated by PCA. Also note that the regression of n principal components means the inclusion of the top n principal components arranged according to their variance as regressors.

Detrending is implemented as part of multiple linear regression step by adding a linear trend as an additional regressor to the general linear model.

Another methodological issue is the order of linear regression and frequency filtering. Hallquist et al. found that applying band-pass filtering to the signal time series before removing nuisance effects can lead to inappropriate control of physiological/movement effects [55]. Therefore, I opted for the reverse procedure, where regression was performed before band-pass filtering.

5.4.3 Results

After all the preprocessing was carried out, the mean correlations were computed within default mode network (DMN) and dorsal attention system (ATT) for serving as signal metrics, among reference regions (primary motor, visual, auditory cortex) as noise metric and among DMN and ATT as anticorrelation signal metric. Before averaging, correlation values were Fisher transformed to obtain z correlation values. Fig.15 displays voxel-wise group level

[15] Software of Gabrieli Lab. McGovern Institute for Brain Research, Massachusetts Institute of Technology: http://www.nitrc.org/projects/conn

z correlation maps with respect to the PCC seed region in 6 slices of the brain and across all the preprocessing approaches. These correlation maps were overlaid on a template anatomical image obtained from the standard library of MRIcroN. Positive and negative correlations were thresholded at 0.1 and -0.1, respectively. The influence of various preprocessing strategies on the sensitivity and specificity of signal metrics are plotted in Figure 16. The specificity is defined according to [43] as:

$$S = \frac{|Z| - |Z_{ref}|}{|Z| + |Z_{ref}|} \tag{34}$$

where Z denotes the signal metric and $|Z_{ref}|$ is the mean correlation among the reference networks (noise metric). Absolute values are necessary to obtain positive specificity values for the anticorrelation metric. Note that specificity of anticorrelation was only calculated if the absolute value of negative correlation exceeded the noise metric.

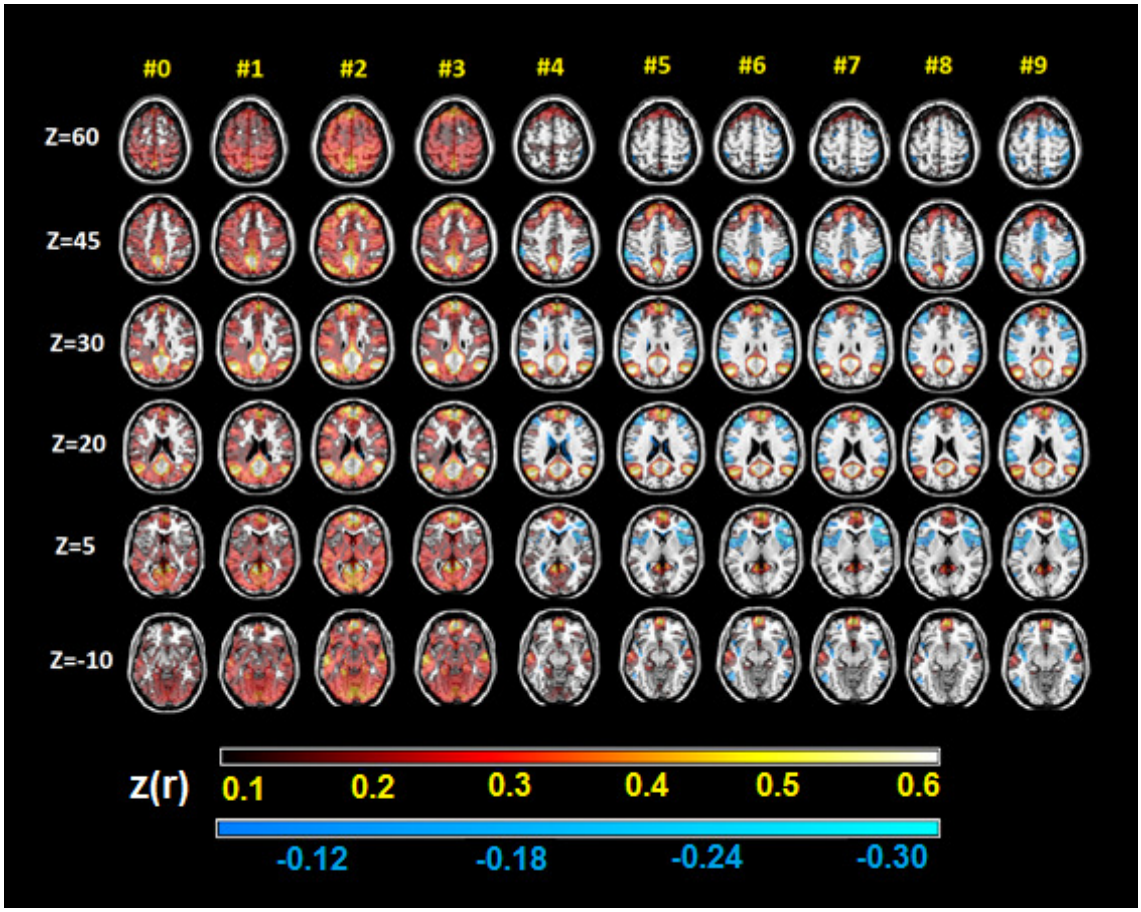

Figure 15. Group-level voxel-wise z correlation maps with respect to PCC seed are displayed in 6 different slices (Z coordinates are given in MNI space) and across all preprocessing strategies. Color-coded correlations (positive values in red, negative values in blue) are overlaid on a standard anatomical volume.

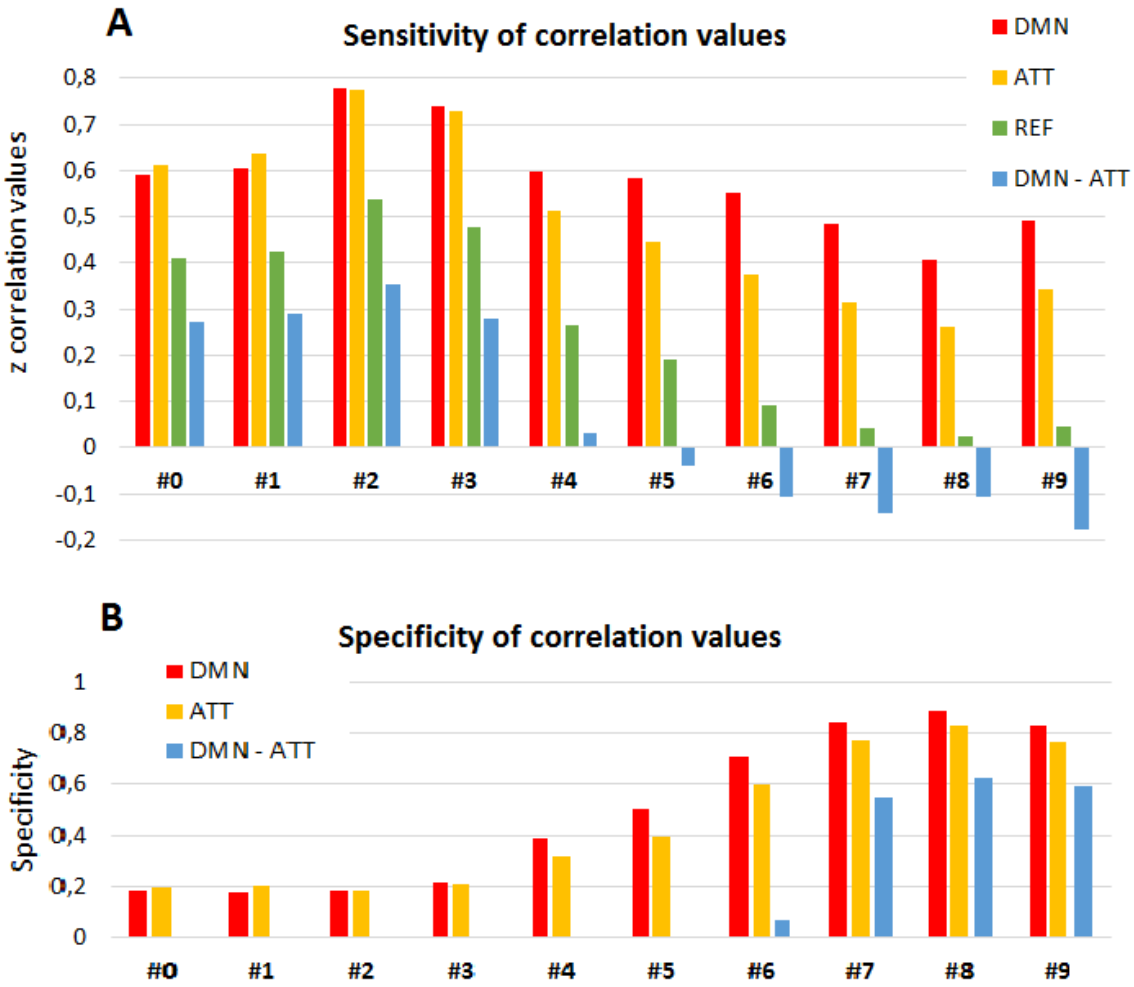

#0: unsmoothed
#1: smoothed
#2: smoothed, band-pass filtered
#3: smoothed, band-pass filtered, corrected for motion
#4: smoothed, band-pass filtered, corrected for motion, mean WM & CSF signal
#5: smoothed, band-pass filtered, corrected for motion, 3 principal components from WM & CSF
#6: smoothed, band-pass filtered, corrected for motion, 5 principal components from WM & CSF
#7: smoothed, band-pass filtered, corrected for motion, 10 principal components from WM & CSF
#8: smoothed, band-pass filtered, corrected for motion, 15 principal components from WM & CSF
#9: smoothed, band-pass filtered, corrected for motion, mean WM & CSF signal, global signal

Figure 16. A: Mean *z* correlation strengths within default mode network (DMN), dorsal attention system (ATT) as well as among reference regions (REF) and between DMN and ATT are plotted against the preprocessing strategies. B: Specificity of the mean correlation within DMN and ATT as well as between DMN and ATT are quantified for each preprocessing strategy.

Figures 15 and 16 clearly demonstrate that preprocessing choices influence the magnitude of correlations. First, high correlations were present even when no preprocessing was applied. The topography of the DMN can be readily observed in Fig.15 (mainly in slices with Z-coordinates of 20 and 30 mm) in the unsmoothed dataset (#0), but there are a lot of non-specific correlations with respect to the PCC seed resulting in a low specificity of real correlations as can be seen in Fig.16B. This inherent low specificity in the seed correlation analysis indicates the need for adequate preprocessing. Also note that valid and meaningful correlations corresponding to LLP, RLP and MPFC were the highest in the unsmoothed dataset suggesting that the threshold can be raised above the level of nonspecific correlations to obtain the real topography of the default mode network.

The blurring effect of smoothing slightly expands the area of voxels exceeding the threshold of 0.1 (#1 in Fig.15). Smoothing has a minor effect on the sensitivity and specificity results, because the calculation of these values already involves signal averaging within ROIs making the additional spatial smoothing redundant. However, if small ROIs or even voxels are used to define nodes of networks, the effect of spatial smoothing can be higher.

Interestingly, the application of band-pass filtering has been found to substantially increase both specific and non-specific correlations. It may be caused by the exclusion of the high-frequency random signal components induced by thermal noise and it results in a further expansion of the correlated area with respect to PPC (#2 in Fig.15) as well as in an increase in the signal and noise metrics. However, since these metrics increase proportionally, the specificity of correlations remains approximately unchanged.

The regression of six motion parameters as well as their first derivatives (#3) does not make significant differences compared to #2. An interesting observation is that contrary to large parts of the WM, the ventricular system does not correlate with the PCC in the cases of #0 - #3, which is most probably caused by the low signal to noise ratio in CSF signals quantified in Section 5.3.1.

Regression against the mean signals from the noise ROIs removed non-specific correlations to a large extent. Correlations of PCC with voxels within the noise ROIs are obviously eliminated, but false correlations with functionally non-related areas in GM are also suppressed resulting in a 1.5-2-fold increase in the specificity results. However, correlations within functional networks are also somewhat reduced reflected in lower sensitivity values in DMN and ATT networks. These observations can be attributed to the fact that coherent fluctuations present in the noise ROIs are also removed from the functional networks.

Regression of 3 principal components (#5) instead of the mean signal from noise ROIs provides better noise control; however, the correlation among the reference networks is still around 0.2. However, when even more principal components are regressed out (5, 10, 15 in the cases #6, #7, #8, respectively), it is further reduced reaching almost zero in #8. It suggests that removing higher number of PCA components is more effective in noise correction, since PCA components represent a more complex set of time series to characterize physiological effects that cannot be captured by a single temporal component. However, the more PCA components are regressed out, the more correlations reduce in DMN and ATT networks, which results in a saturation of positive correlations when regressing out 10 or more PCA components. It is due to the fact that regression against signals from noise ROIs always carries the risk of removing neural signal in functional networks, because neural related signals and PCA components from noise ROIs may share similar characteristics. It is also possible that noise ROIs overlap with functional networks in spite of one-voxel erosion. Even a small contamination of noise regressors with true neural induced signal may be sufficient to reduce specific correlations.

Global signal regression (#9) provided very similar results to the case of #7. Application of this technique instead of aCompCor also increases the specificity results, but this approach is under debate for several reasons discussed in Section 4.3.3. Most notably, the global signal regressor is highly contaminated by the signals of functional networks.

Note that robust, widespread anticorrelated networks (with respect to PCC) were only present after regression of at least 5 principal components or after global signal regression. Some papers argue that anticorrelated networks are artificially induced by global signal regression, but the fact that both aCompCor and global regression yielded anticorrelated networks of similar topography (see Fig.15) contradicts this argument. Negative correlations are significantly smaller in amplitude than positive ones with global signal regression producing the highest anticorrelations. It is not surprising as global signal regression shifts the correlation histogram towards negative values potentially introducing artificial negative correlations. In terms of specificity of negative correlations, cases #7 – #9 yielded similar results.

In summary, adequate preprocessing greatly suppressed spurious correlations and preserved high correlations in DMN and ATT networks at the same time. Without performing any preprocessing, correlation maps were dominated by non-specific correlations and specificity of correlations within these networks was low. Subsequent preprocessing steps (#1 - #7) steadily increased specificity of positive correlations until a saturation above #7. The

aCompCor approach as an alternative of global regression has proven to accurately describe physiological noise processes in gray matter and is able to reduce the confounding effect of noise. However, regression of too many PCA components is not beneficial because it also reduces the detection sensitivity of functional networks. Based on these results, regression of 5 principal components (from now on referred to as aCompCor 5 approach) seems to be a good compromise between sensitivity and specificity of the true positive correlations, which is consistent with the findings of [46] and [47] who proposed regression of 5 and 6 components, respectively.

5.5 Effect of ROI sizes

While performing seed-correlation analysis it is essential to ensure that seed voxels are chosen within a well-defined functional area and these voxels do not overlap with neighboring functional networks. Large ROIs carries the risk of incorporating multiple functional networks, while small ROIs are more susceptible to high spatial frequency signal variations due to the lack of signal averaging.

In the previous section, signal metrics were calculated based on ROIs of 10 mm radius. Here, I performed the same computations using a variety of ROI sizes including 5, 10, 15, 20 mm radius as well as single voxel seed (designated as 0 mm radius). The mean correlation coefficients within DMN and ATT as well as among these networks (DMN - ATT) in case of #6 preprocessing strategy can be seen in Figure 17.

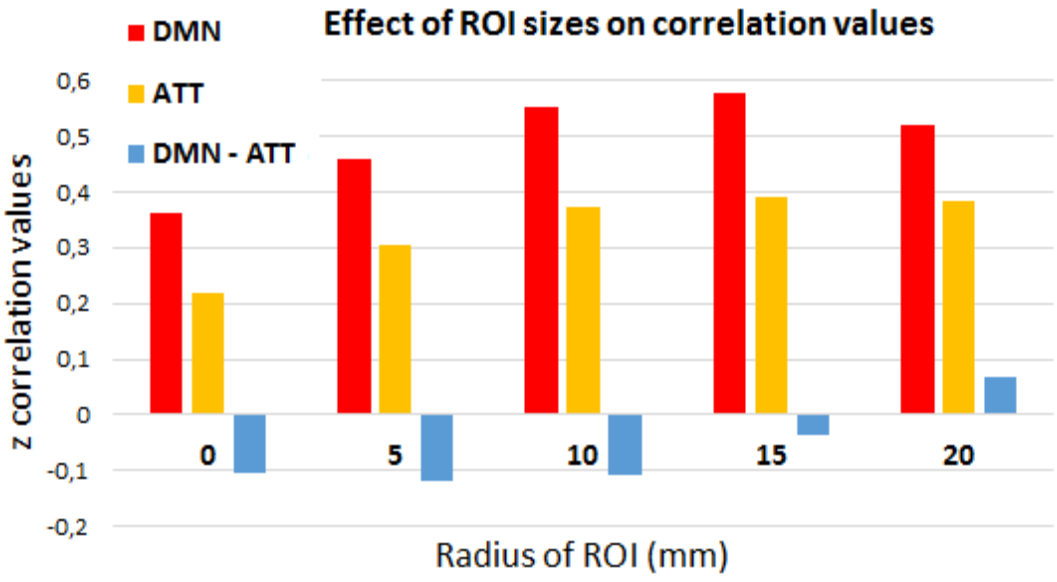

Figure 17. Mean correlation coefficients within DMN, ATT and between DMN-ATT networks in case of the "optimal" aCompCor 5 approach (#6) as a function of ROI size.

Using voxels as seeds have proven to be suboptimal in the detection of functional networks. Positive correlations increase with increasing ROIs and eventually saturate at a radius of 10 mm and higher. Furthermore, a great degradation can be observed in the detectability of anticorrelated networks with increasing ROI sizes. In summary, size of the ROI affects the output of seed-correlation analysis, and according to these results, a ROI radius of 10 mm seems to be optimal.

5.6 Effect of residual motion

Recently, several studies have demonstrated that motion-related effects are not effectively removed by commonly used preprocessing procedures. Power et al. showed that head motion during scans produces substantial changes in the intensity of the BOLD signals across the brain [4]. These intensity changes result from a variety of mechanisms discussed in Section 4.1.2. and can cause systematic but spurious correlation structures throughout the brain. Specifically, spatial blurring due to head motion has been found to increase local, short-range correlation of the signal and decrease the strength of long-range connections with the exception of functionally coupled bilateral brain regions [3]. These results from the literature indicate that head motion significantly affects functional connectivity results including those obtained by SCA. Besides introducing individual changes in functional connectivity, head motion can also create spurious differences between subject groups due to the fact that different subject groups have different level of motion (for examples, patients move more than controls).

Following above considerations, I explored the effect of residual motion on the acquired resting-state dataset of 32 subjects. In Section 5.6.1, measures of head motion and signal intensity changes were computed and their relations were assessed. These metrics characterizing individual level of motion were used to form cohorts, among which group functional connectivity maps were created in Section 5.6.2 to illustrate how head motion might confound an analysis. In Section 5.6.3 the frame-discarding method “scrubbing” proposed by [4] is applied to the data to identify and remove motion-corrupted frames.

5.6.1 Quantification of motion

In order to quantify motion and possibly motion-related intensity changes, it is necessary to define metrics. These measures can be divided into summary measures that describe the whole 4D dataset and into framewise measures that characterize a single frame only.

Absolute displacements of each volume as compared to the previous volume were estimated based on the translational and rotational parameters obtained by the motion correction step (see Section 4.1.2). Rotational parameters were converted into displacements on the surface of the brain by modeling the brain as a sphere of 50 mm radius, which is approximately the mean distance between the cortex and the center of the head. Mean absolute displacement for each subject was also calculated by averaging absolute displacements over all the frames.

Individual mean absolute displacements were used to divide the 32 subjects into 4 groups of equal sizes designated as “low”, “lower middle”, ”higher middle” and “high” motion groups. Mean absolute displacements averaged within each group were (0.0536 ± 0.0094 mm), (0.0756 ± 0.0089 mm), (0.098 ± 0.0063 mm) and (0.1595 ± 0.0487 mm), respectively. Note however, that the mean absolute displacement as a summary measure is not able to distinguish between qualitatively different types of subject movement.

To characterize the framewise change of BOLD signal across the brain, the time series of each voxel was differentiated (by backwards difference) and the resulting absolute signal intensity changes were averaged across the whole brain for each frame of data. Furthermore, mean tSNR was also used as a summary measure to indicate data quality. It was computed by averaging the voxel-wise tSNR within the brain mask for each subject. The association between mean absolute displacement and mean tSNR was explored in Figure 18, where a strong inverse relation between these two measures was found consistent with [3]. It suggests that head motion reduces tSNR by introducing noise in the measurement. To explore which parts of the cortex are most susceptible to motion-induced noise, group-level contrast was created between the high and low motion group by subtracting the two group-averaged voxel-wise tSNR from each other (Figure 19).

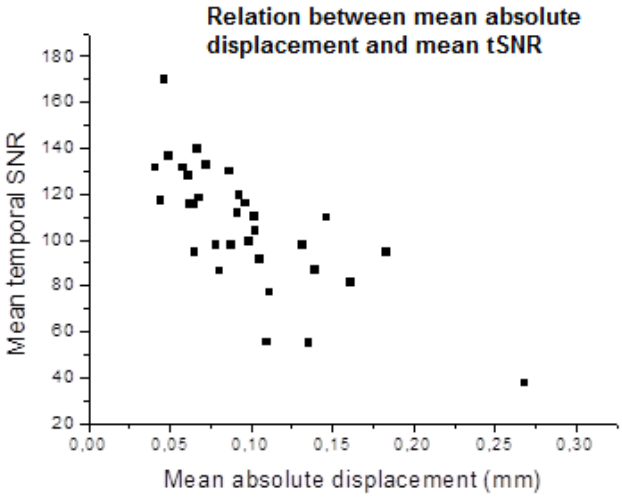

Figure 18. Mean tSNR within the brain mask is plotted against the mean absolute displacement for each subject.

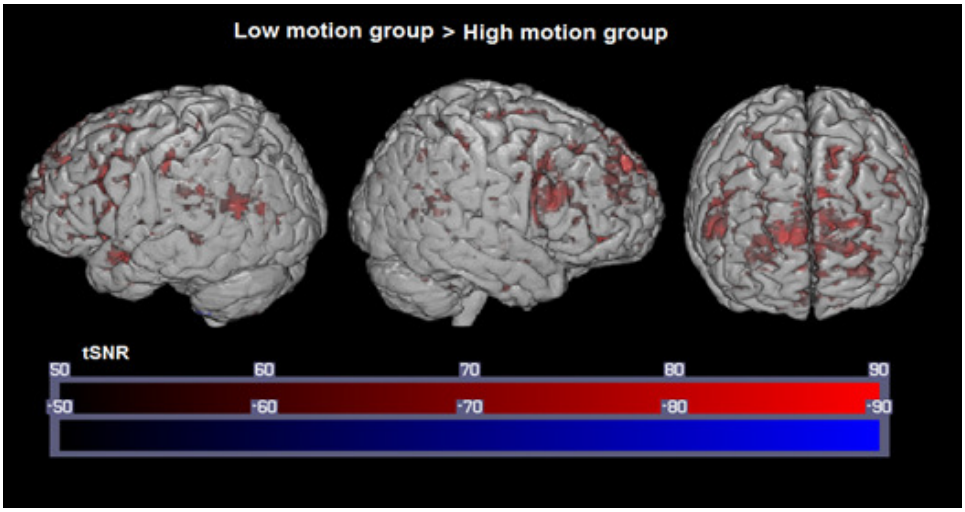

Figure 19. Group tSNR difference map projected onto the surface of a brain template. Areas of high positive (plotted by red) and negative (plotted by blued) differences between the high and low motion group are displayed. Note that there are virtually no areas with significantly higher tSNR in the high motion group.

Fig.19 demonstrates that tSNR is generally lower in the high motion group and the greatest tSNR differences between the two groups are in the prefrontal cortex.

The relation between head motion and BOLD signal changes in a single subject is demonstrated in Figure 20. Fig.20A shows the framewise absolute displacement as a function of time ($TR = 2\ s$). While the subject was relatively still during most of the experiment, several peaks associated with high motion are visible throughout the data that can last even tens of seconds. Figure 20B,C plot the mean absolute intensity change within the brain mask before and after temporal preprocessing (aCompCor 5 approach). The unit of this measure is % as all voxel-wise BOLD signals are intensity normalized to percentage values (see Section 5.4.2).

It is evident that there is a clear correspondence between framewise displacement and signal intensity change, periods of high movement contain substantially changing signals. Although these plots refer to only one subject, similar patterns were found in other subjects, too. The magnitudes of these signal changes are too high to be caused by neuronal activity (e.g. motor related neural activity) suggesting that these peaks reflect in fact motion-related artifacts specified in Section 4.1.2. Note that data are contaminated with artifactual motion-related noise even after performing temporal preprocessing including regression of motion parameters. The reason for the ineffectivity of motion parameter regression to remove motion effects may be that motion causes complex, non-linear signal changes that can also vary across the brain, which cannot be modeled by the simple motion parameter estimates.

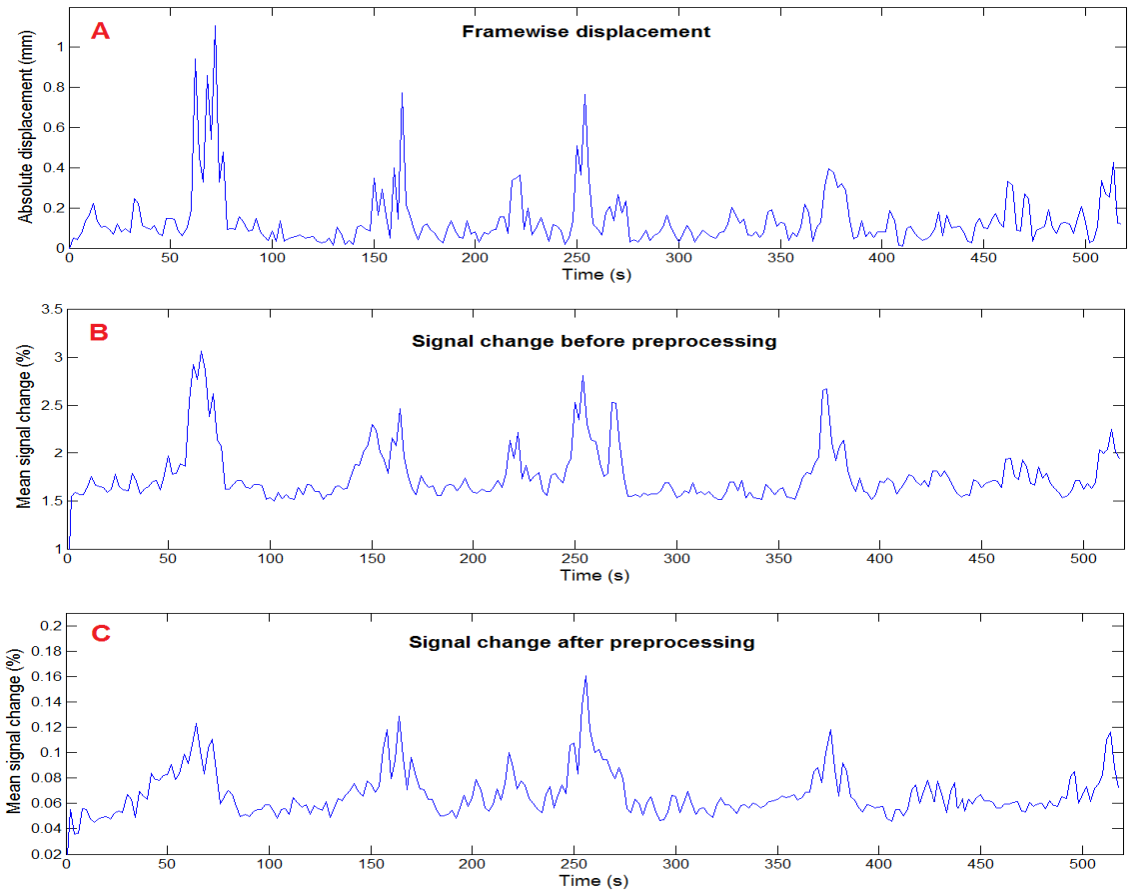

Figure 20. A: Framewise absolute displacement in mm as a function of time. B: Mean absolute BOLD signal change in the unprocessed data over the course of the experiment. C: Mean absolute signal change after preprocessing the data using aCompCor 5 approach.

5.6.2 Between-group connectivity differences

As a demonstrative example how between-subject differences in head motion can affect functional connectivity, group difference correlation maps were constructed between groups defined in the previous section using PCC seed (MNI coordinates: 0, -53, 26). The correlations between the time courses of each voxel and the PCC seed were calculated on preprocessed data (aCompCor 5 approach). Individual correlation maps were averaged within each group and contrasts were formed by subtracting average correlation maps from each other. Such contrasts between high motion vs. low motion groups and between higher middle vs. lower middle motion groups are projected onto a brain template in Figure 21. Besides the contrast map (displayed in red), group-level[16] correlation map (displayed in green) representing the DMN is also projected on the surface to make comparisons easier.

[16] Group-level correlation map was computed by averaging all the 32 individual correlation maps.

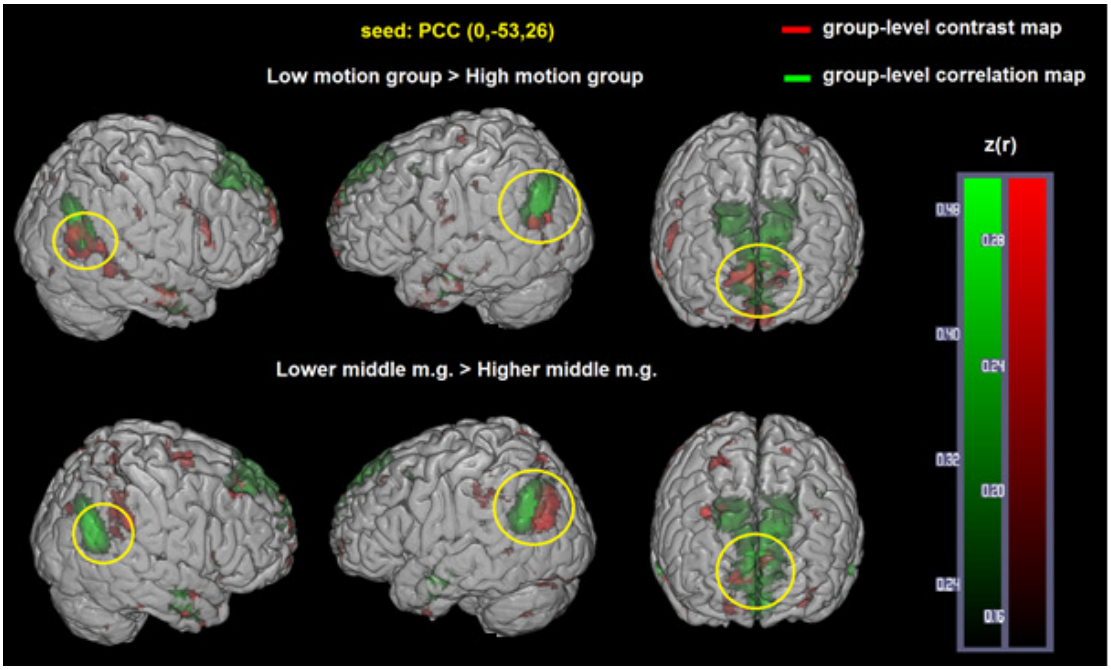

Figure 21. Group difference functional connectivity maps (seed: PCC) between low and high as well as between lower middle and higher middle motion group are displayed in red. Group average correlation map is also overlaid onto the surface and is displayed in green. The overlap or high proximity of the two maps are marked by yellow circles.

The mean correlations in the high motion group were found to be significantly lower in areas that closely resemble the DMN (lateral parietal lobes, medial prefrontal cortex). The high degree of overlap between the group-level DMN network and the group-level difference maps seen in Fig.21 emphasizes that correlations associated with PCC seed are mainly reduced in high motion subjects where high correlation strengths are originally expected. Furthermore, the higher middle motion group also shows decreased connectivity compared to lower middle m. g. in areas that are similar to the pattern of DMN.

In summary, high group-level differences are present when the only known major difference between the groups is the level of head motion. Due to their similar structure to DMN they can be easily misinterpreted as neuronal effects. Since all subjects were clinically normal young adults, even higher differences are expected in patient groups who have significantly higher level of motion. Therefore, it is critical to consider the effect of head motion while interpreting group-level differences, because it may bias between-group studies in the direction of the hypothesized difference.

5.6.3 Scrubbing

Given the functional connectivity differences head motion can produce, it is important to address residual motion artifacts in the signal on a case by case basis. One possible method to reduce residual motion effects is scrubbing first introduced in Power et al., 2012, [4]. Scrubbing attempts to identify and entirely remove frames that are irreversibly corrupted by motion artifacts.

In the first step a temporal mask for each subject was created using the framewise measures defined in Section 5.6.1: absolute displacement and mean absolute signal change across the brain. The idea behind applying simultaneously two indices as exclusion criteria was that although these two measures correlate to a high level (see Fig.20.), the threshold in the signal change may also remove frames that are corrupted by instabilities other than head motion. After studying the plots of all the subjects (an example can be seen in Fig.20.), threshold values were set to 0.25 mm for absolute displacement and 2.2 % for mean absolute signal change in the raw data. Temporal masks for each index and subject contained frames whose framewise measures exceeded these thresholds. Furthermore, temporal masks were augmented by also including frames 1 back and 1 forward from any frames already marked to correct for the temporal smoothness of the BOLD data and to allow for the re-establishment of the spin steady-state. Final temporal mask was created by taking the union of the two masks. The framewise measures of a subject (the same subject as in Fig.20) with the selected thresholds are displayed in Figure 22A and B, while Fig.22C shows the final temporal mask. Note that only those frames are marked whose indexes are well beyond the values found in still periods of the measurement.

Marked frames were removed after preprocessing, because temporal filtering cannot work properly on temporal discontinuous data. However, subsequent seed correlation analysis is thus performed on concatenated discontinuous data, but previous studies found no corresponding detrimental effects on functional connectivity [18]. The mean proportion of data removed from each subject was $\mathbf{13.69}$ %. Similar to Power et al. [4], I presented the requirement that at least 5 minutes of data must remain after scrubbing corresponding to an exclusion proportion of 42.31 %. Two subjects could not satisfy this requirement, they were excluded from all analysis in Sections 5.3-5.5.

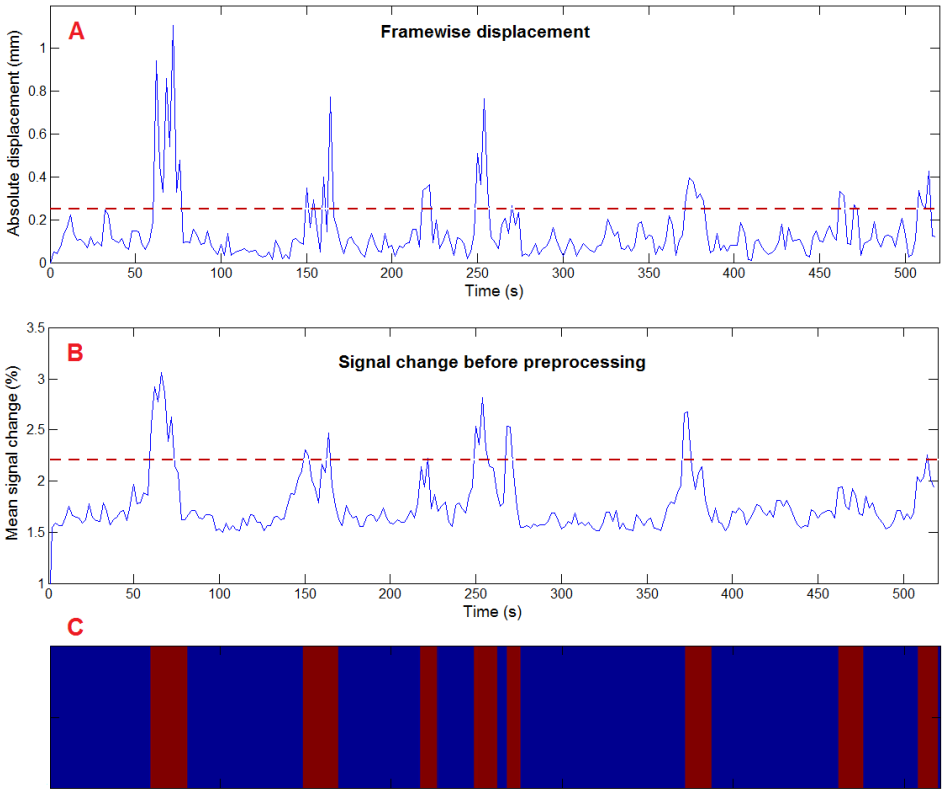

Figure 22. A: Framewise absolute displacement in mm as a function of time with the level of threshold at 0.22 mm. B: Mean absolute BOLD signal change in the unprocessed data with a threshold of 2.2%. C: Final (augmented and united) temporal mask.

In order to test the ability of scrubbing to reduce residual motion artifacts, I created the same group-level contrast as in the previous section (Figure 23). Despite scrubbing, significant connectivity differences were found at similar locations as in Fig.21. It suggests that high group-level connectivity differences between groups with different level of motion still exist after scrubbing. There are several possible reasons scrubbing is not able to remove all motion-related signal. First, even frames with values below the thresholds contain motion-induced signal, but further reducing the threshold is not beneficial because it would remove too much data. Second, applying band-pass filter on motion-corrupted data spreads the compromised signal into non-compromised volumes. However, based on the similar pattern of signal change before and after preprocessing (see Fig.20), this effect is expected to be minor. Third, general linear model is applied to all data including the motion-corrupted volumes, so high-motion periods may present outliers in the regressors also propagating to the parameter estimates and thus resulting in suboptimal performance of the multiple linear regression.

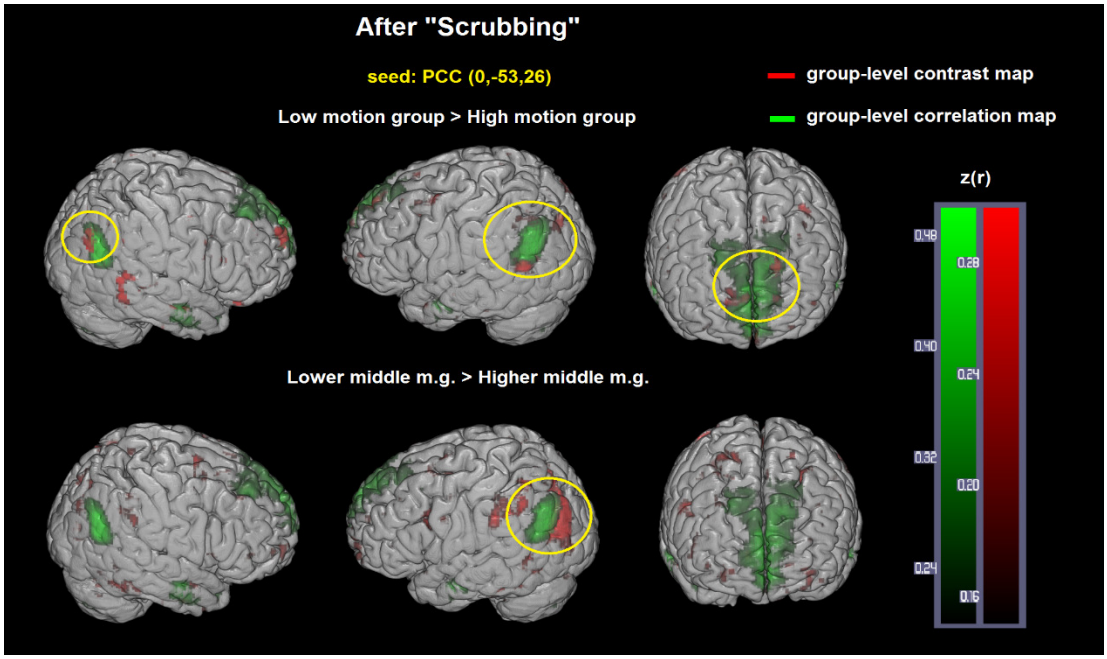

Figure 23. Group difference functional connectivity maps (seed: PCC) between low vs. high as well as between lower middle vs. higher middle motion groups obtained after scrubbing and displayed in red. Group average correlation map is also overlaid onto the surface and is displayed in green. The overlap or high proximity of the two maps are marked by yellow circles.

6. An application of the method: Altered functional connectivity in patients with retrosplenial epilepsy

Functional connectivity has been widely used to explore individual and group differences. Several reports indicate distinct changes in inter-regional functional connection strength in a variety of psychiatric and neurological disorders [15]. As an application of the optimized fMRI preprocessing, I investigated how retrosplenial epilepsy and subsequent tumor excision affects the functional connectome of the human brain. The retrosplenial area is an important hub in the functional architecture of the brain, because it partly overlaps with one of the main nodes of DMN comprising the posterior cingulate cortex and the precuneus. It was expected that disorder or removal of this region severely disrupts the functional connectome. The main question of interest was whether the functional connections of patients who have undergone brain surgery significantly differ from those of normal population.

Data were collected from two patients (designated as Patient #1 and Patient #2) 10 and 15 years after retrosplenial surgery, respectively. In both cases the surgery was performed to remove retrosplenial tumor that caused severe epileptic symptoms. Figure 24 illustrates on the patients' anatomical images that the tumors were in fact in the area corresponding to DMN's posterior node as detected by group-level independent component analysis. The control group representing the normal population consisted of the 30 subjects described in Section 5.1 (2 outliers excluded).

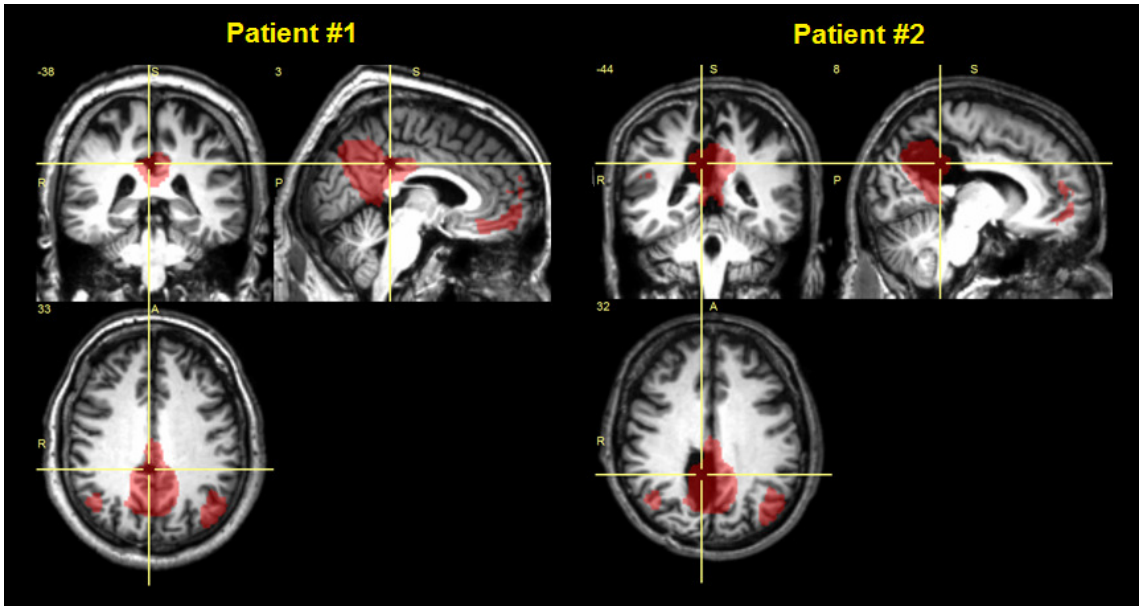

Figure 24. Group-level default mode network shown by red overlaid onto the normalized anatomical image for each patient. In both cases the surgery (indicated by the yellow crosshair) was performed in the area of DMN. Although the location of the lesion is similar in both cases, the size of the lesion in Patient #2 is much larger than that in Patient #1.

The two patients underwent the same resting-state fMRI acquisition protocol specified in Section 5.2. Standard spatial preprocessing (Section 5.2) was performed on the collected fMRI data. Subsequently, data were band-pass filtered between 0.01 Hz and 0.1 Hz, detrended and regressed for realignment parameters as well as 5-5 principal components extracted from the WM and CSF regions, since this procedure has proven to be optimal in terms of sensitivity and specificity of resting-state network detection (Section 5.4.3).

In order to assess the whole-brain functional connectivity, the brain was parcellated based on Brodmann's atlas[17] into 42 non-overlapping segments for each hemisphere and subject. As a regional estimator of the BOLD signal, mean signal was calculated from each of the 84 segments. Then, cross-correlation coefficients were computed among all the regions resulting in an 84 x 84 correlation matrix, in which the ij^{th} element indicates the correlation coefficient between the $i.$ and $j.$ regions. Subsequently, one-sided t-test was performed for each matrix element to determine which pair of regions have significantly different correlation values compared to the control group. Regions that overlapped with the lesion were excluded from the analysis (1 region for Patient #1, 4 for Patient #2). Multiple comparisons correction was performed using the false discovery rate (FDR) approach with $q = 0.05$, which in our case corresponded to $p < 0.02$ uncorrected level of significance, i.e. the chance of false positives causing significant effects is lower than 2%. In the assessment of individual connectivity differences described above, an individual's test score is compared against a normative sample. To account for the small sample size, a modified t-test was used that treats the individual as a sample ($N = 1$):

$$t = \frac{Z_1 - \overline{Z_2}}{s_2\sqrt{\frac{N_2+1}{N_2}}} \tag{35}$$

where Z_1 is the Fisher transformed correlation of the patient, $\overline{Z_2}$ is the mean z-correlation of the normative sample, s_2 is the standard deviation of the normative sample, and N_2 is the sample size. As a result of the hypothesis test a 84 x 84 matrix was obtained for each patient, where the ij^{th} element indicates whether the correlation between the $i.$ and $j.$ regions in the patient is significantly lower or higher than that in the normative sample. These matrices are displayed in Figure 25, where blue and red entries indicate significant increases and decreases, respectively.

[17] Brodmann's atlas of the CONN toolbox found at: conn\rois\BA.img.

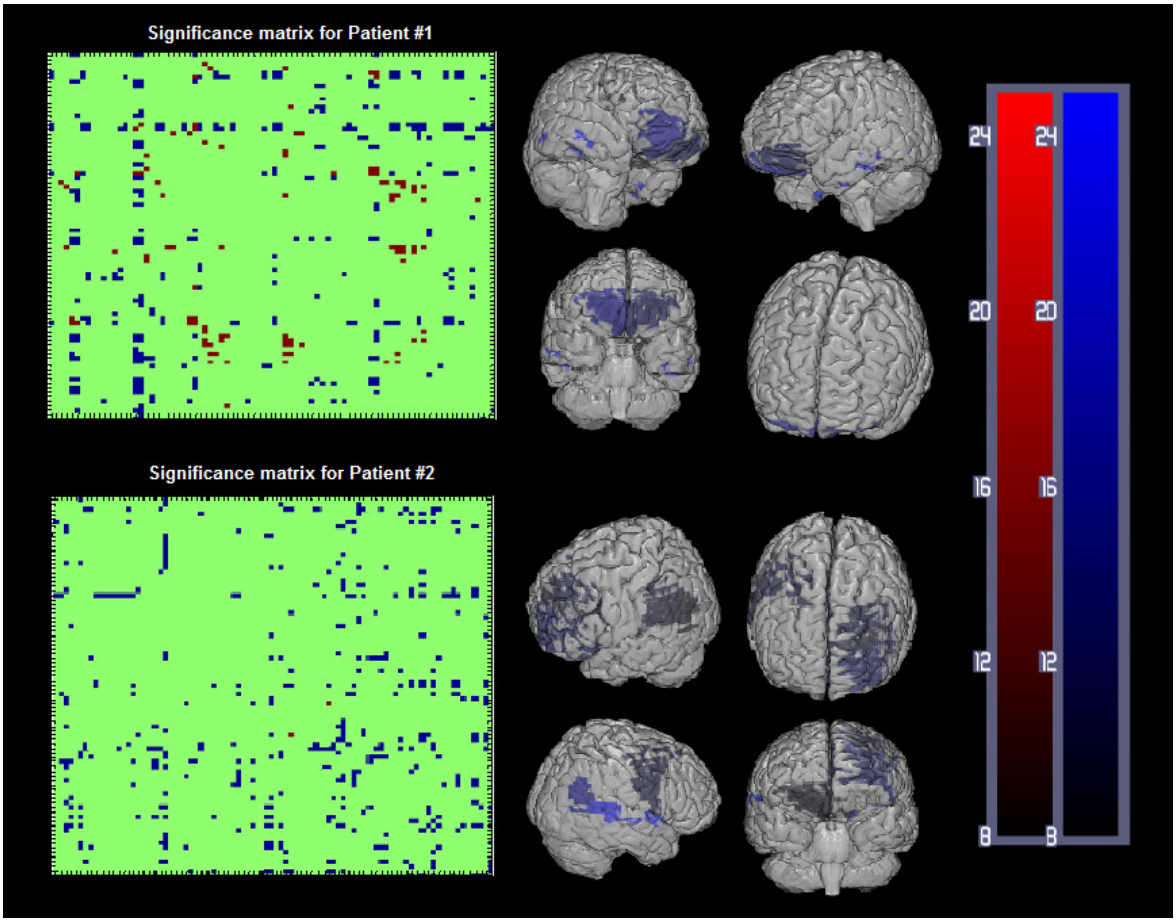

Figure 25. Significance matrices for both patient can be seen on the left (blue entry: significantly low, red entry: significantly high correlation). The Brodmann areas with the most positive or negative entries are displayed on the standard brain surface. Red and blue contrasts represent the number of increased and decreased functional connections associated with the given Brodmann area.

In general, both significance matrices were dominated by reduced correlations. Further, significance matrices reveal several Brodmann areas with highly reduced connection strengths (e.g. orbitofrontal cortices in Patient #1, left prefrontal cortex in Patient #2). Brodmann areas with more than 8 significantly reduced or increased functional connections are plotted onto a standard brain surface in Fig.25. In summary, the existence of several areas with reduced functional connections indicate disrupted connectivity in both subjects caused by either the consequences of the earlier epilepsy or by the tumor excision and resulting lesion itself.

7. Summary and conclusions

The goal of the thesis was to characterize the effect of noise in human resting-state fMRI datasets, and to subsequently find an optimal data processing strategy to mitigate these unwanted effects. First, I confirmed that resting-state datasets do in fact contain considerable fluctuations unrelated to neural processes that cause inflated estimates of functional connections. Then, I explored the ability of several typical preprocessing procedures to increase detection sensitivity and specificitiy of well-known resting-state networks. Processing steps examined were spatial smoothing, band-pass frequency filtering, regression of motion as well as regression of signals extracted from white matter and ventricles.

The results of this thesis demonstrate that performing preprocessing on resting-state fMRI data is necessary to improve detection power of functional brain networks in the context of seed based correlation analysis. Specifically, regression of principal components from noise ROIs using anatomical component based noise correction approach could multiply the specificitiy of correlations in true resting-state networks. However, inclusion of too many principal components has not proven to be beneficial due to saturation of correlation specificity and associated reduction of sensitivity. Based on these results, regression of 5-5 principal components from white matter and ventricles along with band-pass filtering and regression of motion is proposed to be included in the preprocessing stream. In summary, these findings confirm the potential of the aCompCor approach to effectively remove physiological and other noise sources and to serve as an alternative for global signal regression.

I also demonstrated that motion-related fluctuations are not completely countered by these preprocessing procedures. Furthermore, the increasingly applied “scrubbing” procedure wasn’t able to remove all motion-contaminated data either. As a consequence, residual motion artifacts yielded substantial functional connectivity differences between groups with different levels of head motion. It is thus important to consider the confounding effect of noise when interpreting variation between groups and across individuals and further efforts to improve strategies for removing motion artifact is necessary.

As an application of the optimal preprocessing pipeline I investigated the functional connectivity differences between clinically normal subjects and patients with removed retrosplenial tumor. Although the number of patients involved in the analysis was not sufficient to draw well-established conclusions, the results illustrate the potential value of resting-state fMRI to assess individual connectivity differences.

References

[1] Fox, M.D., Snyder, A.Z., Vincent, J.L., Corbetta, M., Van Essen, D.C., Raichle, M.E. The human brain is intrinsically organized into dynamic, anticorrelated functional networks. *Proc. Natl. Acad. Sci. U. S. A.* 102, 9673–9678. (*2005*)

[2] Hampson, M., Peterson, B.S., Skudlarski, P., Gatenby, J.C., Gore, J.C., Detection of functional connectivity using temporal correlations in MR images. *Hum. Brain Mapp.* 2002.15, 247–262.

[3] Van Dijk, K.R.A., Sabuncu, M.R., Buckner, R.L., 2011. The influence of head motion on intrinsic functional connectivity MRI. *NeuroImage* 59 (2012) 431–438.

[4] Power JD, Barnes KA, Snyder AZ, Schlaggar BL, Petersen SE. Spurious but systematic correlations in functional connectivity MRI networks arise from subject motion. *Neuroimage*. 2012; 59:2142–2154.

[5] Website of *Journal of Cardiovascular Magnetic Resonance*: http://www.jcmr-online.com/content/12/1/71/figure/F4 (accessed June 2, 2014)

[6] Website of MRI Imaging: http://mri-imaging.blogspot.hu/ (accessed June 2, 2014)

[7] Website of ReviseMRI.com: http://www.revisemri.com/questions/pulse_sequences/epi (accessed June 2, 2014)

[8] Website of practical fMRI: http://practicalfmri.blogspot.hu/2011/11/physics-for-understanding-fmri.html (accessed June 2, 2014)

[9] Ogawa, S, T Lee, A Kay, and D Tank. "Brain magnetic resonance imaging with contrast dependent on blood oxygenation." *Proc. Natl. Acad. Sci. USA* 87 (1990): 9868-9872.

[10] Website of Oxford Centre for Functional Magnetic Resonance Imaging of the Brain: http://www2.fmrib.ox.ac.uk/education/graduate-training-course/programme/mri-physics/lectures/FMRI_Clare_Basic2011.pdf (accessed June 2, 2014)

[11] Ogawa, S, et al. "Functional brain mapping by blood oxygenation level-dependent contrast magnetic resonance imaging. A comparison of signal characteristics with a biophysical model." *Biophys. J.* 64 (1993): 803-812.

[12] Ugurbil, K., Xiaoping, H., Wei, C., Zhu, X.-H., Kim, S.-G., Georgopoulos, A., Functional mapping in the human brain using high magnetic fields. *Phil. Trans. R. Soc. Lond. B*, 1999, vol. 354 no. 1387 1195-1213.

[13] Website of the Clever Machine (Topics in computational neuroscience & machine learning):https://theclevermachine.wordpress.com/tag/hemodynamic-response-function/

(accessed June 2, 2014)

[14] Huettel, S.A., Song, W.A., McCarthy, G. Functional magnetic resonance.

[15] Lee, M.H., Smyser, C.D., Shimony, J.S. Resting-state fMRI: A Review of Methods and Clinical Applications. 2012 as 10.3174/ajnr.A3263

[16] Biswal B, Yetkin FZ, Haughton VM, Hyde JS. Functional connectivity in the motor cortex of resting human brain using echo-planar MRI. *Magn Reson Med* 34: 537–541, 1995.

[17] Friston KJ. Functional and effective connectivity in neuroimaging: a synthesis. *Hum Brain Mapp* 2: 56–87, 1994.

[18] Van Dijk, K.R., Hedden, T., Venkataraman, A., Evans, K.C., Lazar, S.W., Buckner, R.L., 2010. Intrinsic functional connectivity as a tool for human connectomics: theory, properties, and optimization. *J. Neurophysiol.* 103, 297–321.

[19] Website of Neurology: https://www.neurology.org/content/79/14/1449/F1.expansion.html (accessed June 2, 2014)

[20] Cordes, D., Haughton, V.M., Arfanakis, K., Wendt, G.J., Turski, P.A., Moritz, C.H., Quigley, M.A., Meyerand, M.E., 2000. Mapping functionally related regions of brain with functional connectivity MR imaging. *AJNR Am. J. Neuroradiol.* 21, 1636–1644.

[21] Vincent JL, Kahn I, Snyder AZ, Raichle ME, Buckner RL. Evidence for a frontoparietal control system revealed by intrinsic functional connectivity. *J Neurophysiol* 100: 3328–3342, 2008.

[22] Fukunaga M, Horovitz SG, van Gelderen P, de Zwart JA, Jansma JM, Ikonomidou VN, Chu RX, Deckers RH, Leopold DA, Duyn JH. Largeamplitude, spatially correlated fluctuations in BOLD fMRI signals during extended rest and early sleep stages. *Magn Reson Imaging* 24: 979–992, 2006.

[23] Greicius MD, Kiviniemi V, Tervonen O, Vainionpa¨a¨ V, Alahuhta S, Reiss AL, Menon V. Persistent default-mode network connectivity during light sedation. *Hum Brain Mapp* 29: 839–847, 2008.

[24] Fornito, A., Zalesky, A., Bassett, D.S., Meunier, D., Ellison-Wright, I., Yucel, M., Wood, S.J., Shaw, K., O'Connor, J., Nertney, D., Mowry, B.J., Pantelis, C., Bullmore, E.T., 2011. Genetic influences on cost-efficient organization of human cortical functional networks. *J. Neurosci*. 31, 3261–3270.

[25] Buckner, RL, Andrews-Hanna, JR, Schacter, DL. The brain's default mode network: anatomy, function and relevance to disease. *Ann N Y Acad Sci.* 2008 Mar;1124:1-38. doi: 10.1196/annals.1440.011.

[26] Penny, W., Friston, K., Ashburner, J., Kiebel, S. Statistical Parametric Mapping: The Analysis of Functional Brain Images.

[27] Website of BrainVoyager: *http://www.brainvoyager.com/bvqx/doc/UsersGuide/Preprocessing/SliceScanTimeCorrection.html* (accessed June 2, 2014)

[28] Ashburner, J., Friston, K. Unified segmentation. *NeuroImage* 26 (2005) 839 – 851.

[29] Smith, S.M., Miller, K.M., Salimi-Khorshidi, G., Webster, M., Beckmann, C.F., Nichols, T.E., Ramsey, J.D., Woolrich, W.D. Network modelling methods for fMRI. *NeuroImage* 54 (2011) 875–891

[30] Shehzad Z, Kelly AM, Reiss PT, Gee DG, Gotimer K, Uddin LQ, Lee SH, Margulies DS, Roy AK, Biswal BB, Petkova E, Castellanos FX, Milham MP. The resting brain: unconstrained yet reliable. *Cereb Cortex* 19: 2209–2229, 2009.

[31] Liu, T.T., Neurovascular factors in resting-state functional MRI. *NeuroImage* 80 (2013) 339–348.

[32] Handwerker, D.A., Roopchansingh, V., Gonzalez-Castillo, J., Bandettini, P.A., 2012. Periodic changes in fMRI connectivity. *Neuroimage* 63, 1712–1719.

[33] Hutchison, R.M., Womelsdorf, M., Allen, E.A., Bandettini, P.A., Calhoun, V.D., Corbetta, M., Penna, S.D., Duyn, J.H., Glover, G.H., Gonzalez-Castillo, J., Handwerker, D.A., Keilholz, S., Kiviniemi, V., Leopold, D.A., de Pasquale, F., Sporns, O., Walter, M., Chang, C. Dynamic functional connectivity: Promise, issues and interpretations. *NeuroImage* 80 (2013) 360–378.

[34] Lund, T.E., Madsen, K.H., Sidaros, K., Luo, W.L., Nichols, T.E., 2006. Non-white noise in fMRI: does modelling have an impact? *NeuroImage* 29, 54–66.

[35] Chuang KH, Chen JH. IMPACT: Image-based physiological artifacts estimation and correction technique for functional MRI. *Magn Reson Med* 46: 344–353, 2001.

[36] Niazy, R., Xie, J., Miller, K., Beckmann, C., Smith, S., 2011. Spectral characteristics of resting state networks. In: Van Someren, E. (Ed.), *Progress in Brain Research*, vol. 193. Elsevier, pp. 259–276.

[37] Birn RM, Smith MA, Jones TB, Bandettini PA. The respiration response function: the temporal dynamics of fMRI signal fluctuations related to changes in respiration. *Neuroimage* 40: 644–654, 2008b.

[38] Murphy, K., Birn, R.M., Bandettini, P.A., Resting-state fMRI confounds and cleanup. *Neuroimage*. 2013 Oct 15;80:349-59.

[39] Windischberger, C., Langenberger, H., Sycha, T., Tschernko, E.M., Fuchsjager-Mayerl, G., Schmetterer, L., Moser, E., 2002. On the origin of respiratory artifacts in BOLD-EPI of the human brain. *Magn. Reson. Imaging* 20, 575–582.

[40] Macey PM, Macey KE, Kumar R, Harper RM. A method for removal of global effects from fMRI time series. *Neuroimage* 22: 360–366, 2004.

[41] Hampson, M., Peterson, B.S., Skudlarski, P., Gatenby, J.C., Gore, J.C., 2002. Detection of functional connectivity using temporal correlations in MR images. *Hum. Brain Mapp.* 15, 247–262.

[42] Fox MD, Zhang DY, Snyder AZ, Raichle ME. The global signal and observed anticorrelated resting state brain networks. *J Neurophysiol* 101: 3270–3283, 2009.

[43] Weissenbacher, A., Kasess, C., Gerstl, F., Lanzenberger, R., Moser, E., Windischberger, C., 2009. Correlations and anticorrelations in resting-state functional connectivity MRI: a quantitative comparison of preprocessing strategies. *Neuroimage* 47, 1408–1416.

[44] Murphy, K., Birn, R.M., Handwerker, D.A., Jones, T.B., Bandettini, P.A., 2009. The impact of global signal regression on resting state correlations: are anti-correlated networks introduced? *Neuroimage* 44, 893–905.

[45] Wise RG, Ide K, Poulin MJ, Tracey I. Resting fluctuations in arterial carbon dioxide induce significant low frequency variations in BOLD signal. *Neuroimage* 21: 1652–1664, 2004.

[46] Chai, X.J., Nieto Castanon, A., Öngur, D., Whitfield-Gabrieli, S. Anticorrelations in resting-state networks without global signal regression. *NeuroImage* 59 (2012) 1420–1428.

[47] Behzadi, Y., Restom, K., Liau, J., Liu, T.T., 2007. A component based noise correction method (CompCor) for BOLD and perfusion based fMRI. *Neuroimage* 37, 90–101.

[48] Evans AC, Collins DL, Mills SR, Brown ED, Kelly RL, Peters TM. 3D statistical neuroanatomical models from 305 MRI volumes. *Proc IEEE Nuclear Scie. Symp. Med. Imag. Conf.* 3: 1813–1817, 1993.

[49] Welvaert, M., Rosseel, Y. On the Definition of Signal-To-Noise Ratio and Contrast-To-Noise Ratio for fMRI Data. *PlosOne* DOI: 10.1371/journal.pone.0077089 (2013).

[50] R. M. Birn1, K. Murphy, J. Bodurka, P. A. Bandettini. The use of multiple physiologic parameter regression increases gray matter temporal signal to noise by up to 50%. *Proc. Intl. Soc. Mag. Reson. Med.* 14 (2006).

[51] Ferguson, A. A review of the physiology of cranial osteopathy. *Journal of Osteopathic Medicine*, 2003, 6(2): 74-88.

[52] E. Zarahn, G. K. Aguirre, M. D'Esposito. Empirical Analyses of BOLD fMRI statistics. *NeuroImage* 5, 179–197 (1997).

[53] De Luca, M., Beckmann, C.F., De Stefano, N., Matthews, P.M., Smith, S.M., 2006. fMRI resting state networks define distinct modes of long-distance interactions in the human brain. *NeuroImage* 29, 1359–1367.

[54] Buckner RL, Andrews-Hanna JR, Schacter DL. The brain's default network: anatomy, function, and relevance to disease. *Ann NY Acad Sci* 1124:1–38, 2008.

[55] Hallquist, M.N., Hwang, K., Luna, B. The nuisance of nuisance regression: Spectral misspecification in a common approach to resting-state fMRI preprocessing reintroduces noise and obscures functional connectivity. NeuroImage 82 (2013) 208–225

Acknowledgments

First and foremost, I would like to thank my supervisors, Dr. Lajos R. Kozák and Szabolcs Dávid for the continued support and advice they have provided during the writing of this thesis. Under their guidance I was able to stay focused, structured and motivated over the last one and a half year.

I also thank Dr. Ádám Szabó and in turn, Dr. Lajos R. Kozák for sharing me the data I used throughout the thesis.

I give my sincere thanks to Prof. Péter Halász for his kind help in providing information about the investigated patients.